

Adaptive frequency-based modeling of whole-brain oscillations: Predicting regional vulnerability and hazardousness rates

Neda Kaboodvand^{1,*}, Martijn P van den Heuvel², Peter Fransson¹

¹Department of Clinical Neuroscience, Karolinska Institutet, Stockholm, Sweden.

²Connectome Lab, Department of Complex Trait Genetics, CNCR, VU Amsterdam, The Netherlands.

*Corresponding author

Department of Clinical Neuroscience

Karolinska Institutet

Nobels väg 9

SE-171 77 Stockholm, SWEDEN

E-mail: Neda.Kaboodvand@ki.se

Keywords: resting-state fMRI, brain modeling, dynamical systems, adaptive frequency, In-silico perturbation, vulnerability

Short title: Adaptive frequency-based modeling of whole-brain oscillations

Abstract

Whole-brain computational modeling based on structural connectivity measures has shown great promise in successfully simulating fMRI BOLD signals that includes temporal co-activation patterns that are highly similar to empirical functional connectivity patterns during resting state. Importantly, previous studies have shown that spontaneous fluctuations in co-activation patterns of distributed brain regions have an inherent dynamic nature with regard to the frequency spectrum of intrinsic brain oscillations. In this modeling study, we introduce frequency dynamics into a system of coupled oscillators, where each oscillator represents the local mean-field model of a brain region. We first show that the collective behavior of interacting oscillators reproduces previously shown features of brain dynamics. Our analysis of static and dynamic measures of simulated BOLD fMRI signals support the notion that the frequency of each oscillator is modulated by flow of activity in its neighborhood. Second, we examine the effects of simulated lesions in gray brain matter by applying a new perturbation protocol to our model. We present a new approach to map the effects of vulnerability in brain networks and introducing a measure of regional hazardousness based on mapping of the degree of divergence in a feature space consisting of graph theoretical measures.

Author summary

In this study, we propose a macroscopic computational model of the brain oscillations for resting-state fMRI, in which the frequency of each brain region is modulated by the degree of activity flow in its neighborhood. In particular, regional oscillation frequencies undergoes the highest change where the activity in the neighborhood is in the vicinity of zero, so that the speed of frequency changes reaches its maximum positive value (speed-up) when the net neighborhood activity gets close to the zero, whereas it gets its maximum negative value (slow-down) when the net neighborhood activity has just started to grow. We show that the

collective behavior of interacting oscillator systems in our proposed model reproduces the key features of brain dynamics. By applying an off-line perturbation protocol to our proposed model, we present a spatial map for vulnerability and hazardousness rates.

1. Introduction

The human connectome is a complex network that is made up of interactive systems encompassing a large number of regions. Regions communicate with each other in order to share and process information providing the structural and functional basis for complex cognitive processes. Understanding the network architecture of human brain in the context of its robustness and the integration between different subnetworks (known as functional systems) has received increased attention in system-level network neuroscience. However, we still have limited knowledge of the emergence of brain dynamics from the underlying anatomy. So far, there is evidence suggesting that the large-scale structural connectome of the brain constrains the strength and persistence of resting state functional connectivity (FC) (C J Honey et al., 2009), with significant contributions of structural connections for the integrated state (Fukushima, Betzel, He, van den Heuvel, et al., 2018). An impaired structural connectome may lead to disrupted FC which contributes to neurodegenerative diseases, for example (Griffa, Baumann, Thiran, & Hagmann, 2013). The interplay between the brain's structure and dynamics underlies all brain functions spanning from consciousness and perception to learning, memory and movement (Deco, Jirsa, Robinson, Breakspear, & Friston, 2008). Moreover, the relationship between the structural backbone and the dynamics of brain activity is believed to play an important role for surviving network communication failures and attacks (Barabási, 2016). In the past decade we have witnessed great progress towards the systematic modeling of the neural network dynamics (Breakspear, Heitmann, &

Daffertshofer, 2010; Cabral, Kringelbach, & Deco, 2014; Fink, 2018; Kuramoto, 1984). Large-scale computational models are uniquely suited to address difficult questions related to the role of the brain's structural network in shaping measures of FC averaged across longer time-scales (Cabral et al., 2014; Ritter, Schirner, McIntosh, & Jirsa, 2013). Additionally, we can study the emergence of complex brain dynamics (Roberts et al., 2018), through time-varying analyses of functional coherence.

Several resting-state studies have shown that there exist spontaneous fluctuations in co-activation patterns of distributed brain regions (Hutchison et al., 2013; Thompson, Brantefors, & Fransson, 2017; Zalesky, Fornito, Cocchi, Gollo, & Breakspear, 2014), which gives rise to an efficient information exchange while minimizing metabolic expenditure (Zalesky et al., 2014). Furthermore, spectral analysis of brain fluctuations has disclosed valuable information about the underlying sources of time-varying connectivity of brain regions (C. Chang & Glover, 2010; Ries et al., 2018; Yaesoubi, Allen, Miller, & Calhoun, 2015). These studies suggest that the frequency spectrum of intrinsic oscillations of the brain have a time-varying nature.

In this study, we present a theoretical framework for modeling large-scale brain dynamics based on the theory of dynamical systems. The proposed model is used to show that important questions related to the prediction of perturbation patterns related to the topological structure of the brain's network architecture can be tackled in an accessible and useful way. Furthermore, we show that our model can be employed to simulate perturbations in different brain regions to assess the vulnerability and hazardousness of individual connections and brain regions.

To do this, we start by constructing a macroscopic computational model of the brain where local brain regions, each modeled by a local mean-field model, are interacting through the

structural brain network architecture (Breakspear, 2017; Cabral et al., 2014; Deco & Jirsa, 2012; Deco, Jirsa, McIntosh, Sporns, & Kötter, 2009; Gollo, Zalesky, Hutchison, van den Heuvel, & Breakspear, 2015; C J Honey et al., 2009; Christopher J Honey, Kötter, Breakspear, & Sporns, 2007). We then suggest that the local dynamics of each brain area can be described by a modified Stuart-Landau equation. Subsequently, we show that simulated BOLD signals are forming FC patterns that are highly similar to the FC patterns generated by the measured BOLD signals. This similarity was found to be valid both in terms of strength of FC and in the form of the establishment of communities of brain regions as shown in previous resting-state networks studies (Yeo et al., 2011). Additionally, we show that temporal structure of simulated BOLD signals is highly similar to the fluctuations of empirical BOLD signals.

Of note, by perturbing different brain regions in our model and measuring how the system responds to the induced failures, we can obtain information on the underlying association between structure and dynamics in the brain. Previous studies have simulated the effects of brain lesions on both local and global levels of network activity, for example by removing individual connections (edges) or all connections of an individual region from the network (Cabral et al., 2012a; Vasa et al., 2015; Aerts et al., 2016; Deco et al., 2017c). However, in this study we take a different approach by using an off-line perturbation protocol to the computational model of the brain by applying bifurcation-induced shifts in the dynamical regime for the model of each individual brain region. Regime refers to the characteristic behavior of a dynamical system and regime shifts are sudden, large and persistent changes in the function of the system as a result of some external source of disturbance (Folke et al., 2004; Holling, 1973; Scheffer, Carpenter, Foley, Folke, & Walker, 2001). Therefore, to study the effects of brain lesions, we simulated the effect of malfunction in a brain region by shifting that region's regime away from an oscillatory to a noisy domain of dynamics. Static

as well as dynamic measures of FC patterns were investigated for different in silico failures. This analysis was followed up by applying the representational similarity analysis (RSA) framework to investigate how a targeted brain region's failure contributed to an increased distance between the perturbed connectome versus the healthy connectome in RSA space. Based on the findings presented, we argue that our suggested modeling approach provides an opportunity to quantify of distance between the undisturbed and the perturbed brain connectome. Further, we suggest that the aforementioned distance in turn provides useful information of the degree of hazardousness in each brain region. Moreover, we propose that our approach to modeling brain dynamics is helpful to understand the diversity of fragility for brain regions in the connectome with regard to injuries and disease. Additionally, we suggest that investigating perturbation maps which are aggregated from different types of perturbation targets is a useful marker to estimate the degree of individual regions' and/or connections' vulnerability in the brain connectome.

Quantification of perturbation patterns provided by dynamical systems modeling of the brain may become a helpful tool when designing goal-directed interventions such as presenting sensory stimuli and artificial interventions like applying transcranial magnetic stimulation. Furthermore, given the promising results of new closed loop brain stimulations which are based on ongoing brain activity (Weerasinghe et al., 2018), we believe that a mathematical model of the brain oscillations will be helpful in designing an optimal stimulation strategy that provides detailed information about the particular state of the system which is required. It may also allow us to better understand why some brain lesions cause cognitive and physical impairment that may become more severe over time while other lesion patterns have a much a better long-term outcome.

2. Materials and Methods

2.1. Data used and preprocessing

The primary data source for this study was the Human Connectome 500 subject release (Smith et al., 2013; Van Essen et al., 2012). Subject recruitment procedures and informed consent forms were approved by the Washington University institutional review board. The dataset is publically shared on the ConnectomeDB database (<https://db.humanconnectome.org>). Resting-state fMRI data were collected in two sessions, each session including two runs with phase encoding in either left-to-right or right-to-left directions. For our analysis, we used a single resting-state run, collected during 14.4 minutes with temporal resolution of 0.72 s. The entire dataset consisted of 1200 image volumes.

The dataset had been minimally-preprocessed (Glasser et al., 2013; Smith et al., 2013; Van Essen et al., 2012), which starts with gradient distortion correction and proceeds by realignment, bias field correction, spatial distortion removal, registration to standard Montreal Neurological Institute (MNI) space and intensity normalization (Glasser et al., 2013). Also, ICA+FIX ("FMRIB's ICA-based X-noiseifier") pipeline had been applied in order to automatically remove nuisance components (e.g., motion effects, non-neuronal physiology and scanner artefacts) from the fMRI data (Griffanti et al., 2014; Salimi-Khorshidi et al., 2014). Further preprocessing steps were added to the pipeline. The volumes collected during the first 10 seconds of the scan as well as the outlier volumes were discarded. Using the 3dDespike function in AFNI, outlier volumes were detected and interpolated from neighboring volumes. Next, the nuisance regression was performed using the global signal, mean white matter and cerebrospinal fluid (CSF) signals, as well as the 24 motion time-series (C.-G. Yan, Craddock, Zuo, Zang, & Milham, 2013) simultaneously with linear and quadratic detrending. In addition, the data was band-pass filtered (0.02–0.12 Hz)

(Fukushima, Betzel, He, de Reus, et al., 2018). Moreover, the Freesurfer software (<https://surfer.nmr.mgh.harvard.edu>) was applied to parcellate the cortical surface of T1-weighted images into 68 anatomically segregated gyral-based regions-of-interest (Desikan et al., 2006). This data-driven parcellation is also known as the 'Desikan-Killiany' cortical atlas.

High-quality diffusion-weighted MRI data for the same 500 subjects from the HCP consortium (Glasser et al., 2013; Van Essen et al., 2012) was used for a streamline tractography on 68 cortical regions (Yeh, Wedeen, & Tseng, 2010). Next, we created subject-level weighted structural connectomes using measures of streamline density, computed by dividing the number of streamlines connecting two regions by the average of the volumes of the two interconnected regions to obtain streamline density (Hagmann et al., 2008; van den Heuvel, Kahn, Goñi, & Sporns, 2012; van den Heuvel & Sporns, 2011). For details on the processing steps of diffusion-MRI derived connectivity data we refer the reader to the earlier work (van den Heuvel & Sporns, 2011). We constructed a group-representative structural connectome by averaging the subject-level structural connectivity entries which had nonzero values for at least 60% of the subjects (de Reus & van den Heuvel, 2013), followed by resampling the data to follow a Gaussian distribution with $\mu = .5$ and $\sigma = .15$ (C J Honey et al., 2009; van den Heuvel et al., 2015).

2.2. Computational modeling of brain dynamics

In our system-level model of the brain, each region was modeled by a local mean-field model and they interact with each other through the structural connectome as previously described (Breakspear, 2017; Cabral et al., 2014; Deco & Jirsa, 2012; Deco et al., 2009; Gollo et al., 2015; C J Honey et al., 2009; Christopher J Honey et al., 2007). Accordingly, we model the local dynamics of each brain area with a modified Stuart-Landau equation. The Stuart-Landau equation describes the behavior of a nonlinear oscillating system near the Hopf

bifurcation and it can be thought of as the principal model for nonlinear oscillators since it is the simplest possible model to describe amplitude dynamics (Röhm, Lüdge, & Schneider, 2018). When coupled together, the collective behavior of interacting oscillator systems has been shown to reproduce features of brain dynamics (Deco, Kringelbach, Jirsa, & Ritter, 2017; Freyer et al., 2011). Graph theory allows representing the interactions within the resulting complex network through a set of nodes which are connected by edges (M. E. J. Newman, 2003; Rubinov & Sporns, 2010; S H Strogatz, 2001). Nodes in a graph/network represent brain regions, while edges may represent either structural or functional connections. Since we are modeling the neural activity of each brain region with the oscillations produced by an oscillator's model, the words "brain region", "node" and "oscillator" will be used interchangeably in the text.

2.2.1. Local-field mean model

The Stuart-Landau equation describes the dynamic behavior of each oscillator (region) j by:

$$\dot{z}_j = \left(a + i\omega_j - |z_j|^2 \right) z_j \quad (1)$$

where $z = r e^{i\theta} = r \cos \theta + ir \sin \theta$ is a complex number describing the state of the oscillator, $\omega \in \mathbb{R}$ is the frequency of each oscillator and the bifurcation parameter $a \in \mathbb{R}$ determines whether the oscillator is characterized by noisy fluctuations or exhibits oscillatory behavior. In a dynamic system, fixed points (steady states) of the system are all points where there is no flow in the system ($\dot{z} = 0$), representing equilibrium solutions. The origin (i.e., $z = 0$) is the fixed point for all parameter values of this system. Fixed points can be categorized by an evaluation of the signs of the eigenvalues at these points, which subsequently helps in determining the qualitative behavior of the system in the neighborhood of fixed points. The eigenvalues of our system all have complex conjugate values ($\sigma = a \pm$

$i\omega$), indicating a spiral trajectory behavior in phase space. Therefore, the equilibrium points are either spiral sinks (if $a < 0$) or spiral sources (if $a > 0$). In other words, if $a < 0$, then the origin is a stable equilibrium solution with solutions spiraling into the origin. However, if $a > 0$, then the origin is an unstable equilibrium with solutions spiraling out from the origin (Hilborn, 2000; Kuramoto, 1984; Steven H. Strogatz, 2018). An illustrative example of phase space vector fields as well as temporal evolution of the Stuart-Landau oscillator is provided in Supplementary Figure 1.

By applying a slight change to the control parameter (a) of the nonlinear system, an abrupt qualitative change in the behavior of the system may occur, which is called bifurcation. For example, if the control parameter (a) in equation (1) moves from the negative to the positive domain, a critical point is reached when the pair of complex eigenvalues for the oscillator crosses the imaginary axis. At this bifurcation point, the equilibrium of the system loses its stability and a closed orbit (known as limit cycle) of radius \sqrt{a} with a constant angular frequency ω develops, which is called a Hopf bifurcation. The closed orbit in the phase space represents the periodic behavior of the system. Solutions that reside inside of the closed orbit will spiral out towards the orbit, while solutions outside of the orbit will spiral inward. In the Stuart-Landau equation, a negative sign of $|z|^2$ can immediately predict the type of Hopf bifurcation as a supercritical form of Hopf bifurcation, indicating that at the critical point of the system a stable periodic solution will emerge when the equilibrium solution destabilizes (Hilborn, 2000; Kuramoto, 1984; Steven H. Strogatz, 2018).

Nonlinear dynamic models with stable limit cycles describe systems with self-sustained oscillations (i.e., oscillating behavior persists even in the absence of external periodic forcing or facing with slight perturbations). It is intuitively clear that inside a stable limit cycle, there must be an unstable equilibrium point, since neighboring trajectories spiral toward the limit

cycle. In addition, such non-linear systems are required to have complex conjugate eigenvalues to ensure a spiral behavior in phase space. The non-linear system described above is easier to analyze if we rewrite the equation (1) in polar coordinates, which in turn give us the equations below:

$$\xrightarrow{z=re^{i\theta}} \begin{cases} \dot{r}_j = ar_j - r_j^3 \\ \dot{\theta}_j = \omega_j^0 \end{cases} \quad (2)$$

If we translate the model state in equation (2) to functional neuroimaging data, we can interpret the real part of the variable z (i.e., $r \cos \theta$) as the derivative of brain activity acquired by the MR scanner, whereas the imaginary part serves as the hidden state of the system that is unobservable.

2.2.2. Modeling whole brain dynamics — Collective neurodynamics

The next step is to embed the local dynamics for each node as postulated in equations (1) and (2) into a large-scale model that encapsulates all nodes in the brain connectome. Then, the dynamics of whole brain is described by a system of coupled differential equations as given below:

$$\dot{z}_j = (a + i\omega_j - |z_j|^2)z_j + G \sum C_{ij}(z_i - z_j) \quad (3)$$

In equation (3), $G \in \mathbb{R}$ is the global coupling parameter where the strength of coupling between regions is set by the structural connectivity matrix C that governs the interaction strength among different regions. In order to assure that the model is well behaved in the thermodynamic limit of $N \rightarrow \infty$ as well as to keep the parsimony of the model, we assume that the structural connectivity between all regions in the brain have the same conductivity parameter (Arenas, Díaz-Guilera, Kurths, Moreno, & Zhou, 2008; Deco et al., 2017; Rodrigues, Peron, Ji, & Kurths, 2016). Therefore, the constant G serves as a common tuning

parameter that scales all the connection weights similarly. If the global coupling parameter is set into the weakly coupled oscillator limit, the limit cycle of the individual oscillators will be preserved which defines the interval of validity for the aforementioned differential equations (Deco et al., 2017).

In addition, additive Gaussian noise (denoted with η_j with standard deviation of $\beta=0.02$ and implemented as Wiener process), was added to the differential equation of each oscillator to simulate the effect of random processes that occur in brain (e.g., stochastic effects of ion channels and heat), as well as inputs from sensory systems that have not been explicitly modeled (Roberts, Friston, & Breakspear, 2017).

2.2.3. Introducing frequency dynamics (freely running frequency evolution)

As mentioned earlier, it has been shown that the frequency spectrum of intrinsic oscillations of the brain have a dynamic nature (C. Chang & Glover, 2010; Ries et al., 2018; Thompson & Fransson, 2015; Yaesoubi et al., 2015). We therefore describe the dynamics of angular frequency for every area j as:

$$\dot{\omega}_j = \omega_j^0 - \lambda \omega_j \quad (4)$$

where we introduce the coefficient $\lambda \in \mathbb{R}$ as the frequency lethargy. For brain region j , the angular frequency ω_j represents the free running frequency, and ω_j^0 is its intrinsic frequency. The intrinsic frequency for brain region j was estimated from the actual BOLD signals of that particular region, as given by the median (across subjects) peak frequency of the mean (across voxels) BOLD signal.

Notably, in this study we introduce the possibility of frequency modulation of each oscillator in the model, where the oscillating frequency can be modulated by its neighbors (we will later show that the frequency change for each region can be modulated by the net phase of all

oscillators in its direct neighborhood). Thus, by combining the previous model of whole brain dynamics (as formulated in equation 3) with the suggested frequency modulation equation we arrive at the following coupled differential equations to describe the whole brain dynamics in the connectome:

$$\begin{cases} \dot{z}_j = \left(a + i\omega_j - |z_j|^2 \right) z_j + G \sum C_{ij} (z_i - z_j) + \beta \eta_j \\ \dot{\omega}_j = \omega_j^0 - \lambda \omega_j + m \psi_j \end{cases} \quad (5)$$

The global phase of the neighbor ensemble for oscillator j is denoted by phase angle ψ_j , which represents the interacting phases of the ensemble of all oscillators connected to this particular oscillator. Additionally, the model stated in equations (5) includes the frequency modulation coefficient m , which needs to be optimized for the BOLD data. The frequency modulation term was introduced to test the hypothesis that it could offer a suitable platform to understand the dynamic organization of synchronization patterns in the brain connectome.

In our model, frequency modulation is achieved through the structural connectivity matrix so that for each oscillator it limits the inclusion of oscillators in the neighbor ensemble to the ones which are directly structurally connected to that particular oscillator ($\psi_j = \sum C_{ij} \theta_i$). This implies that only neighboring oscillators that are directly structurally connected may have an effect on the frequency change for that particular oscillator. The phase of each oscillator (denoted by θ_i) was calculated as the inverse tangent of the quotient of dividing the imaginary part by the real part of the system variable (z_i).

2.3. Identification of the optimal working point for the model

The optimal working point for the model requires a maximum of similarity between the empirical and simulated BOLD signals. The global coupling parameter G and the global bifurcation parameter a , frequency lethargy coefficient λ and the frequency modulation

coefficient m are the control parameters of our model which are required to be optimized in order to find a working point where the simulated signals maximally fit the empirical BOLD signals. We performed a grid-search framework to estimate optimal values for model parameters. Maximum fitness was achieved by minimizing the dissimilarity between model-driven measures and the metrics extracted based on the empirical BOLD signals. Measures of interest included time-averaged measures like the Pearson correlation of static FC patterns and modularity which quantifies the level of segregation for the resting-state subnetworks, as well as three measures calculated based on instantaneous phase of signals. We computed a composite score by converting each metric to a unity-based normalized distance between model and empirical data and subsequently averaging them. Applied methods for computation of these measures are summarized below:

2.3.1. Measures based on time-averaged functional connectivity

Static functional connectivity patterns

The matrix of correlation coefficients was computed from the pre-processed BOLD signals originating from all 68 regions-of-interest as included in the 'Desikan-Killiany' cortical atlas. Subsequently, the Fisher's r -to- z transformation was applied to each subject's connectivity matrix. A group-level FC matrix was calculated by averaging the subject-level connectivity matrices. The Pearson correlation coefficient between the group-level FC matrix and the FC matrix obtained for the simulated signals was used as one of the measures indicative of similarity between empirical and simulated BOLD signals.

Whole brain modularity

Previous research have found functional networks/systems as ensembles of brain regions that co-activate during resting-state as well as during tasks (Smith et al., 2009). In order to

associate every region of brain with a functional network, we first overlaid the 68 regions with the functional networks (so called “resting-state networks”) which were previously defined based on the similarity of intrinsic FC profiles in 1,000 subjects (Yeo et al., 2011). Based on the percentage of overlap, we related each region with one of the functional networks. Accordingly, the 6 functional networks considered here included the default mode network (DM), the limbic network (LIM), the dorsal attention or control network (dTT/CONT), the salience or ventral attention network (SAL/vATT), the somatomotor network (SOM) and the visual network (VIS). Supplementary Figure 2 displays the layout of these functional networks. The used abbreviations for brain regions are shown in Supplementary Table 1.

On the other hand, the whole brain network/graph can be divided into subnetworks of highly connected nodes, often termed as modules or communities, indicating some commonality or specialization of function. Each module comprises nodes which are more densely connected to each other than to nodes residing in other modules (Betz et al., 2014; Fornito, Zalesky, & Bullmore, 2016; Rubinov & Sporns, 2011). Indeed, the brain network contains several modules that are in good agreement with known functional systems (Meunier, Lambiotte, Fornito, Ersche, & Bullmore, 2009; Power et al., 2011). The presence of these modules that correspond to the functional systems is an indication that the brain network adequately models some characteristics of brain organization.

Modularity quantifies the degree to which a network can be divided into the groups of nodes (i.e., modules) with stronger intra-module connections and weaker inter-module connections.

For a FC matrix with positive weights, modularity is defined as:

$$Q = \frac{1}{v} \sum_{i,j} (w_{ij} - \frac{s_i s_j}{v}) \delta_{ij} \quad (6)$$

where the i, j -th element of the FC matrix is denoted by w_{ij} , and $s_i = \sum_j w_{ij}$ is the nodal strength. The variable $v = \sum_{ij} w_{ij}$ is the overall weight of the network. The Kronecker delta function δ_{ij} is equal to one if the i -th and j -th nodes belong to the same module, and 0 otherwise. Hence, we computed the modularity (Q) of whole-brain network, assuming the abovementioned functional networks (DM, LIM, dATT/CONT, SAL/vATT, SOM, and VIS) being the network's modules.

2.3.2. Instantaneous phase-based measures

Here, we applied the Hilbert transformation to the regional BOLD signals to derive the analytic representation of the real-valued BOLD signals. The Hilbert transformation can be thought as convolution of the Cauchy kernel with the input signal implemented as a multiplication in Fourier domain. We calculated the instantaneous phase of the analytic signal by computing the four quadrant inverse tangent (\tan^{-1}) of the quotient formed by dividing the imaginary part by the real part of the BOLD signal.

Dynamic functional connectivity patterns

Functional coupling between interacting oscillators has a time-varying/dynamic nature (Hutchison et al., 2013; Pedersen, Omidvarnia, Zalesky, & Jackson, 2017; Thompson et al., 2017; Zalesky et al., 2014). Computing the instantaneous phase synchrony (phase coherence) as a measure of time-varying FC offers single time-point resolution and has gained considerable attention in the recent literature (Córdova-Palomera et al., 2016; Demirtaş et al., 2016; Glerean, Salmi, Lahnakoski, Jääskeläinen, & Sams, 2012; Omidvarnia et al., 2016; Pedersen, Omidvarnia, Walz, Zalesky, & Jackson, 2017; Ponce-Alvarez et al., 2015). The instantaneous FC for each pair of regions was defined by cosine similarity of the phases obtained from associated regions' signals. Thus, it was computed as $1 - |\sin(\Delta\theta)|$ at each

time-point, where $\Delta\theta$ represents the instantaneous phase difference between two BOLD signals.

Next, the similarity between instantaneous FC measures of different time-points was calculated based on the cosine similarity between vectors created by applying half-vectorization on every instantaneous FC matrix. The cosine similarity of each pair of instantaneous FC vectors can be derived by dividing the Euclidean dot product of two vectors by their associated magnitudes which results in a matrix of size 1200×1200 for each subject. Half-vectorization (due to the symmetry of these matrices) was employed followed by concatenation of vectors across all subjects. Next, we selected the cumulative distribution of the result (combined measures) as a measure of dynamic connectivity (Deco et al., 2017; Senden, Reuter, van den Heuvel, Goebel, & Deco, 2017). The same procedure was applied to the simulated data.

As a final step, we applied the Kolmogorov-Smirnoff test, which reports the greatest distance between the two cumulative distributions, to evaluate the degree of agreement between dynamic FC patterns obtained by the empirical BOLD data and the results generated by our model. This comparison was performed for all tested combinations of the control parameters in the model.

Macroscopic coherence of the model system

At the edge of the critical point of the bifurcation in a system of coupled oscillators, there is a transition of the global attractor from incoherence to synchrony (Skardal, Ott, & Restrepo, 2011), which can be defined through the emergence of a macroscopic mean-field. This mean-field is computed as the centroid vector of the phase distribution as:

$$R = r \exp(i\phi) = \frac{1}{N} \sum_{j=1}^N \exp(i\theta_j) \quad (7)$$

The amplitude of the centroid vector (indicated by the scalar r) represents the phase divergence or uniformity of N oscillators and ϕ is the representative phase of the set of oscillators (Breakspear et al., 2010). Importantly, r describes the global phase coherence of the system at each time-point as it disappears when the phases of oscillators have large circular variance and approaches one when all the oscillators moving nearly in phase (Breakspear et al., 2010). It is customary to describe the global dynamic behavior of the ensemble using the mean and the standard deviation of r across time-points, which are referred to as the global synchrony and global metastability, respectively (Cabral, Hugues, Sporns, & Deco, 2011; Váša et al., 2015). Metastability refers to the existence of a form of “winnerless competition” between two apparently opposing tendencies, namely, a tendency of individual oscillators to couple with each other and coordinate globally for multiple functions, and a tendency to be independent to express their specialized functions (Kelso, 2008; Roberts et al., 2018; Tognoli & Kelso, 2014). Put differently, a system with either complete synchronization or complete asynchronization has no metastability (metastability = 0), whereas coherence-incoherence transitions produces a higher value of metastability (Shanahan, 2010). We computed global synchrony and global metastability as indicative of macroscopic coherence of the whole-brain network model, for all tested combinations of the control parameters. In addition, we calculated these measures for the empirical BOLD signals (Supplementary Figure 4). We calculated the distance between empirical and simulated global synchrony and metastability in order to evaluate their agreement.

2.4. Perturbation assessment

We simulated perturbation to every individual brain region in our model by shifting the dynamic regime of the targeted region from the oscillatory dynamics domain (characterized by the estimated bifurcation parameter) to the noise-driven fluctuations (characterized by

negative values for bifurcation parameter such as $a = -2$). This shift has the effect that the activity in the targeted region to a larger extent is characterized by a noisy behavior. With regard to investigating the effects from perturbations, we took advantage of the mathematical representation of the brain network as a graph with a set of nodes symbolizing brain regions and edges denoting the mutual interactions among nodes (M. E. J. Newman, 2003; Rubinov & Sporns, 2010; S H Strogatz, 2001). Using the graph-theoretical framework, it is possible to estimate various key measures of the brain as a whole (e.g., global efficiency), its subnetworks (e.g., segregation) or individual nodes (e.g., centrality measures), to characterize different aspects of the network (Harary, 1969; M. Newman, Barabási, & Watts, 2011; Rubinov & Sporns, 2010; Sporns, Honey, & Kötter, 2007; van den Heuvel & Sporns, 2013).

2.4.1. Robustness — network breakdown under random failures versus targeted attacks

Robustness refers to the capacity of a system to absorb disturbances caused by either internal or external faults and still maintaining its basic structure and function, even if some nodes and edges may be missing (Barabási, 2016). Due to the scale-free structure of brain networks (Barabasi & Albert, 1999), it has been shown that failure of hub regions in the brain (“targeted attacks”) have more detrimental effects on the network structure compared to “random failures” (Barabási, 2016). To test the performance of our model with regard to targeted attacks versus random failures, we simulated perturbation of every individual region by setting the bifurcation parameter to $a = -2$. An increasing fraction of regions, as denoted by f , were selected and perturbed, followed by measuring the size of largest strongly connected component (so called “giant component”) formed in the network (Barabási, 2016). In an undirected graph, two nodes belong to the same component if there is at least one sequence of edges connecting them. The presence and absence of edges are denoted by binary edges. Therefore, giant component size was measured after applying a binary

classification of the edges into two groups (0: disconnected or 1: connected) on the basis of a classification rule (i.e., threshold). We tried 100 different thresholds (0-1) for the binary classification of the static FC matrices which were computed based on either the empirical BOLD data (empirical FC) or the simulated BOLD data (using optimal parameter settings).

Next, we computed the accuracy of the binary classification test at every threshold (Supplementary Figure 3). Accuracy was determined by dividing the number of correct assessments (number of true positives + number of true negatives) into the number of all assessments (number of true/false positives + number of true/false negatives). As illustrated in Supplementary Figure 3, the application of conservative thresholds resulted in that the accuracy of binarization increases at the expense of precision. Precision is the number of true positive assessments divided by the number of all positive assessments (number of true/false positives) returned by the classifier. Finally, after we fitted the cubic polynomial curve to the precision values (illustrated as the dotted green curve in Supplementary Figure 3), we estimated the location of the knee of both curves to be 0.27. Therefore, keeping connections stronger than 0.27, provides us high values of accuracy and precision. Additionally, the intersection point of the two curves gives the threshold of 0.08 which is a more liberal threshold compared with the aforementioned knee point. It is worth mentioning that applying a common absolute threshold to the perturbation maps (as models of impaired brain connectome) is preferred to relative thresholding in the literature (Fornito et al., 2016).

Testing the robustness of our modelled brain network was performed using two different perturbation strategies: (1) Simulating random failures by applying perturbations to an increasing fraction of regions which were randomly selected. This procedure was repeated many times ($n = 2000$) while the random number generator was reseeded at each iteration. (2) Simulating targeted attacks by applying perturbations to an increasing fraction of regions which were already sorted according to their degree of centrality in the structural connectivity

matrix. That is, regions with a higher centrality were targeted for perturbation before the remaining regions. The degree of centrality of each region was measured as a composite hub-score that was calculated by averaging the unity-based and normalized measures of nodal strength, betweenness centrality and closeness centrality (Freeman, 1977, 1978; Kaboodvand, Bäckman, Nyberg, & Salami, 2018; Rubinov & Sporns, 2010; Sporns et al., 2007; van den Heuvel & Sporns, 2013). Compared to nodal strength which is basically the number of connections between a given node and the other nodes in a network, betweenness and closeness centrality are computed based on shortest path in the network. Betweenness centrality of a node measures the proportion of shortest paths among all of the other nodal pairs that pass through that particular node, while closeness centrality of a node is an indication of the shortest path lengths between network nodes and that particular node. A node with the strongest closeness centrality has the shortest path length to all the other nodes. Graph nodes with the highest betweenness centrality mediate the most proportion of information transfer within a network (Kaboodvand et al., 2018).

2.4.2. Vulnerability mapping — assessment of the functional connectivity changes subject to distributed failures

The susceptibility of a networked system to undergo significant changes in its function when confronted with different forms of disruption is called vulnerability. Applying perturbations to different regions of the network, and subsequently analyzing the perturbation patterns, is called vulnerability mapping which aims to locate weaknesses within the system (Gollo et al., 2018). After applying the perturbation to every individual region of the brain network separately, we ended up with 68 sets of whole-brain network time-courses, each set simulating the brain with malfunction in one of the 68 brain regions. In addition, we had one set of simulated signals corresponding with the healthy brain which was modeled at optimal working point (see above). First, we computed the static FC matrices for every set of whole-

brain signals (68 sets corresponding to simulated perturbations and one set for the optimal working point). Subsequently, we computed the nodal strength (i.e., sum of connection-weights) of every node, followed by measuring the relative difference of nodal strength vector derived for every perturbation set, from the nodal strength vector yielded by the unperturbed set. Hence, we obtained 68 relative difference vectors, each representing the percentage change in nodal strength patterns caused by an induced single-node perturbation. Then, we aggregated the positive and negative values of percentage changes, separately. This was done in order to measure two different types of nodal vulnerability: nodal hyper-connectivity (bias to increase FC) and nodal hypo-connectivity (bias to decrease FC).

In addition, inter-network FC between each pair of functional networks (DMN, LIM, CONT/dATT, SAL/vATT, SOM and VIS networks) was computed by averaging FCs among all node-pairs belonging to different functional networks (Kaboodvand et al., 2018). To compute the link vulnerability, we first subtracted the inter-network FC matrices derived for every perturbation set from the inter-network FC matrix yielded by the unperturbed set, followed by dividing the subtraction result into the FC matrix of the unperturbed set. Hence, we obtained 68 normalized divergence maps, each representing the percentage change in inter-network FC patterns caused by an induced single-node perturbation. Next, we aggregated the positive and negative values of normalized divergence maps, separately. This was done in order to measure two different types of link vulnerability: link hyper-connectivity and link hypo-connectivity risks.

In the case of hyper-connectivity, both the relative difference vectors and the relative divergence maps were binarized by retaining the values stronger than 50 percentile of the positive entities, followed by computing the average of binary values (which gives the percentage for hyper-connectivity). On the other hand, for the case of hypo-connectivity, both the relative difference vectors and the relative divergence maps were binarized by retaining

the values lower than the 50 percentile of the negative items, followed by computing the average of resulting binary values (which gives the percentage for hypo-connectivity).

2.4.3. Hazard mapping — assessment of the hazardousness of different brain regions

In addition to the three instantaneous phase-based measures which were used for finding the optimal model parameters, we calculated static FC-based measures including the global efficiency of whole brain network, system-wise local efficiency and the level of segregation for every functional system separately. Measures of the global and local efficiency were normalized by a matched (preserved degree distribution) random null model. Aforementioned measures were computed for the model of healthy brain (one set of whole-brain time-courses corresponding to optimal simulated brain) as well as for 68 models of the impaired brain (68 sets of whole brain time-courses corresponding to simulated local perturbations). Each measure was unity normalized across 69 observations. Subsequently, static FC-based measures were recruited to create a 13-dimensional feature vector for every simulated perturbed/unperturbed set of whole-brain signals. The vector space associated with these 69 feature vectors is called the feature space. In a similar way, we created a 3-dimensional feature space for instantaneous phase-based measures.

If we apply a perturbation to any region of the brain, it is likely to cause a feature space divergence from the optimal simulated brain network. We refer to the relationship between the location of each perturbation and the level of distance in feature space as hazard mapping, while the measured distance indicates the degree of hazardousness for that particular location. We computed the pairwise Euclidean distance between the feature vectors obtained from the simulated perturbation sets and the feature vector of simulated healthy brain to investigate how every region's failure (representing a lesion in brain) contributes to increasing the

dissimilarity between the simulated impaired brain and the simulated healthy brain. The Euclidean distance between two feature vectors is the square root of the sum of squared differences between corresponding elements of two feature vectors. The level of distance was separately computed for the static FC-based measures and instantaneous phase-based measures. In the case of dynamic connectivity pattern (which is a time-varying measure), the Kolmogorov-Smirnoff distance between cumulative distributions of the pairwise similarity among instantaneous functional connectivity, obtained from the simulated impaired brain and the simulated healthy brain, was used as the numerical difference of their values. Afterwards, the two Euclidean distance measures were unity-based normalized and then summed together to create one distance measure for every perturbation.

We suggest that quantification of the distance between the optimal and perturbed models of the brain serves as a simple measure of regional hazardousness (i.e., the hazard rate which is caused by failure in this region). In other words, a region shows a significant level of hazardousness if applying the perturbation to that particular region causes a substantial level of dissimilarity between the measures obtained from the simulated perturbation set and with the measures calculated for the simulated healthy brain. A brain region with the highest level of hazardousness may be interpreted as the region with the lowest level of fault tolerance.

3. Results

3.1. Model fitting and frequency dynamics

The control parameters of the model (i.e., a, G, λ and m) were estimated in a grid-search framework, extended to a four-dimensional space. We performed a grid search in two steps using a different granularity in each step. First, we used a coarse-grained search that spanned a wide range of values for each parameter. Then, we used the results from the first search to perform a second, more fine-grained search for the optimal choices of a, G, λ and m . From the

first search, we found evidence supporting our hypothesis that resting brain operates at the edge of a critical point of bifurcation, with bifurcation parameters being close to zero produced a better fit of the model. In the fine-grained grid search, frequency modulation coefficient m ranged from 0.1 to 0.2 in 11 steps and frequency lethargy λ ranged from 0.2 to 1 with a step-size of 0.2. The grid-search for the global coupling G included 15 evenly distributed values in the interval of 0.002 to 0.03. The spanning range for the global bifurcation a included 71 values in the range from minus to plus 0.07.

Subsequently, we defined the optimal working point of our model to be the set of parameters that minimized the composite distance score which was calculated as the average of five unity-based normalized distance measures. Making the composite distance score involved subtracting the Pearson correlation of static FC and modularity from one. Figure 1 illustrates the grid-search landscapes of global bifurcation a and global coupling G for five different measures of interest, separately for our proposed frequency modulation-based model versus coupled Stuart-Landau oscillators. The optimal choice of global coupling (G), bifurcation parameter (a), frequency lethargy λ and frequency modulation m is shown as a white asterisk in the first panel of Figure 1 ($G = 0.01$, $a = 0.038$, $\lambda = 0.4$ and $m = 0.14$). The optimal parameter-set is where the level of modularity of the model and the Pearson correlation between static FC derived from the model and empirical data is high. At the same time, the Kolmogorov-Smirnov distance between cumulative distributions of the pairwise similarity among instantaneous FC values, obtained from the empirical and simulated BOLD signals, as well as from the differences of metastability and synchronization of simulated signals from the average metastability and synchronization measures of empirical data is considerably low.

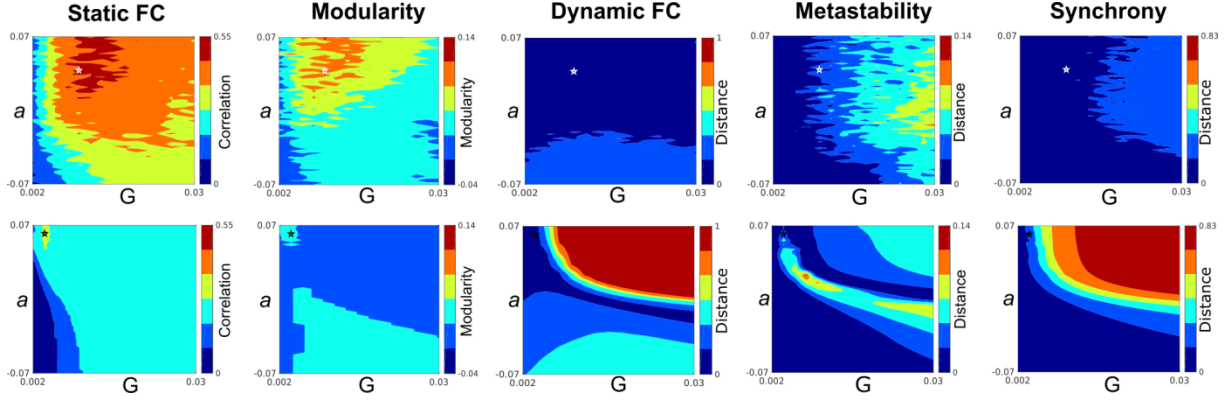
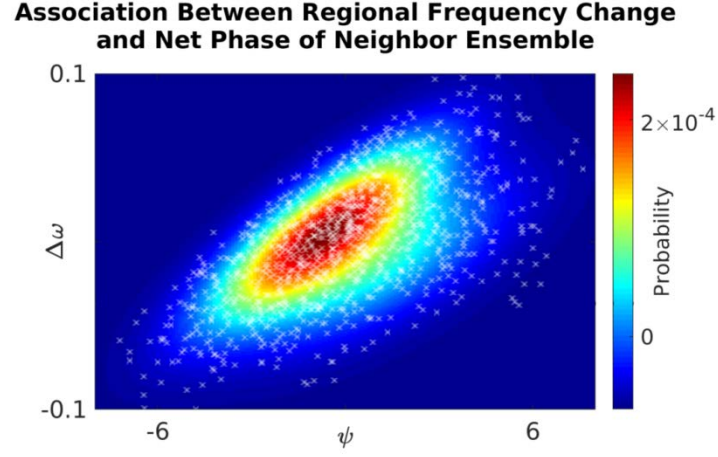


Figure 1. Parameter space search. This figure shows the exploration of the parameter space defined by the bifurcation parameter \mathbf{a} and global coupling \mathbf{G} , separately for our suggested frequency modulation-based model (first row) versus coupled Stuart-Landau oscillators (second row). Measures in the upper panel are reported at the optimal values of frequency lethargy $\lambda = 0.4$ and frequency modulation $\mathbf{m} = 0.14$. First column depicts the Pearson correlation between empirical and simulated static FC patterns for different pairings of bifurcation parameter \mathbf{a} and global coupling \mathbf{G} . Second column shows the whole brain modularity computed for the simulated static FC matrix. The Kolmogorov-Smirnoff distance between cumulative distributions of the pairwise similarity among instantaneous FC values, obtained from the empirical and simulated BOLD signals, as well as the difference of metastability and synchronization of simulated signals from the average metastability and synchronization measures of empirical data are respectively illustrated in columns 3-5. Measures associated with the optimal choice of global coupling (\mathbf{G}), bifurcation parameter (\mathbf{a}), frequency lethargy λ and frequency modulation \mathbf{m} are shown as a white asterisk in the upper panel ($\mathbf{G} = 0.01$, $\mathbf{a} = 0.038$, $\lambda = 0.4$ and $\mathbf{m} = 0.14$), whereas the optimal point for the classic coupled Stuart-Landau oscillator is depicted by a black asterisk in the lower panel ($\mathbf{G} = 0.004$, $\mathbf{a} = 0.062$). See Supplementary Figure 4 for corresponding parameter search maps for frequency lethargy λ and frequency modulation \mathbf{m} .

In the proposed model of the brain oscillations, the frequency of each brain region is modulated by the net phase of the neighbor ensemble. Figure 2a shows the positive association between net phase of the neighbor ensemble and change of frequency in the case of the right precuneus (chosen for illustration purposes). The frequency of a region undergoes the highest change when net phase of the neighbor ensemble reaches its extremum. In other words, the highest frequency change rate is yielded for region j when the net phase of its neighbor ensemble $\psi_j = \sum C_{ij} \theta_i$ reaches its extremums. On the other hand, phase of each neighbor oscillator (denoted by θ_i) is related to the activity of that particular oscillator (i.e., $r_i \cos \theta_i$). Figure 2b illustrates how phase of left posterior cingulate cortex (an example of a neighbor of the right precuneus cortex) is associated with the level of activity.

The phase of oscillator begins to grow when the magnitude (i.e., absolute value) of its activity starts to shrink and it approaches the maximum value (illustrated by light green upward-pointing triangles in Figure 2b) when the magnitude of its activity is passing zero (illustrated by empty circles in Figure 2b). In other words, when the absolute value of overall activity in the neighborhood of region j starts to decline, the net phase of the neighbor ensemble (ψ_j) begins to grow until the overall neighborhood activity passes zero and starts to regrow again. Therefore, the net phase of the neighbor ensemble (ψ_j) reaches its maximum value (light green upward-pointing triangles in Figure 2b) at the point where the overall neighborhood activity is at the minimum level (empty circles in Figure 2b). In conclusion, the frequency of a region (e.g., right precuneus cortex) undergoes the highest change when the net activity of its neighbor ensemble is in the vicinity of zero, so that the speed of frequency changes reaches its maximum positive value (speed-up) when the net neighborhood activity gets close to pass the zero line, whereas it gets its maximum negative value (slow-down) when the net neighborhood activity has just started to grow.

a)



b)

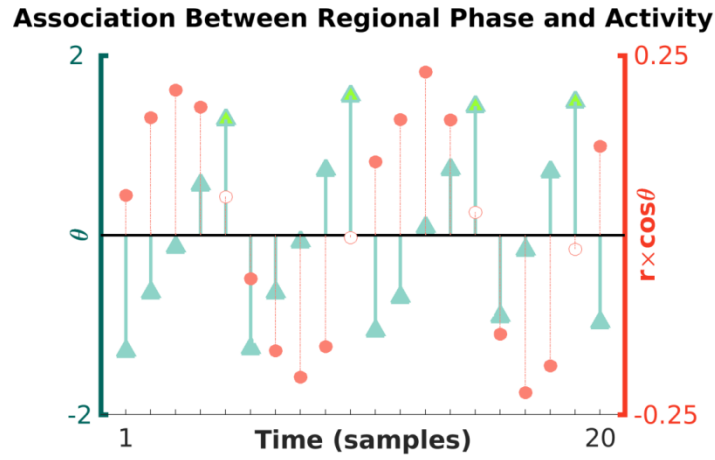


Figure 2. Frequency dynamics in the proposed model of brain oscillations. (a) There is a positive association between the net phase of neighbor ensemble and change of frequency of a region. The right precuneus cortex was selected for illustration purposes. In order to better illustrate the relationship between the net phase of neighbor ensemble and the change of frequency, we fitted a Gaussian mixture model on the simulated data. The probability distribution for the Gaussian mixture model across two components (i.e., net phase of neighbor ensemble and change of frequency) is depicted in the first panel. (b) Association between the phase (θ) of left posterior cingulate cortex (an example neighbor of the right precuneus) and its level of activity ($r \times \cos \theta$). Phase of each individual oscillator (θ) is related to the activity of that particular oscillator, as defined by ($r \times \cos \theta$). The phase of oscillator begins to grow when the magnitude of its activity starts to shrink and it approaches

the maximum value (illustrated by light green upward-pointing triangles in Figure 2b) when the magnitude of its activity is going to pass the zero value (illustrated by empty circles in Figure 2b).

3.2. Robustness, vulnerability and hazard mapping for the whole-brain network model

As a measure of network robustness, Figure 3 displays the fraction of brain regions that belong to the giant component after applying either random or targeted (hubs) perturbations to an f fraction of regions. The size of the giant component at every value of f was divided by the actual size of giant component (i.e., size of giant component at $f = 0$), which provides a relative measure of giant component size. We defined robustness of the network as the required percentage of perturbations to destroy the network (decrease the size of the giant component below 50% of the actual size). From Figure 3 it can be seen that in the face of random failure, the fragmentation process is gradual. However, the whole-brain network has a lower tolerance when facing with selective attacks to hub regions. Thus, our simulated brain network shows lower degree of robustness for targeted attacks versus random failures.

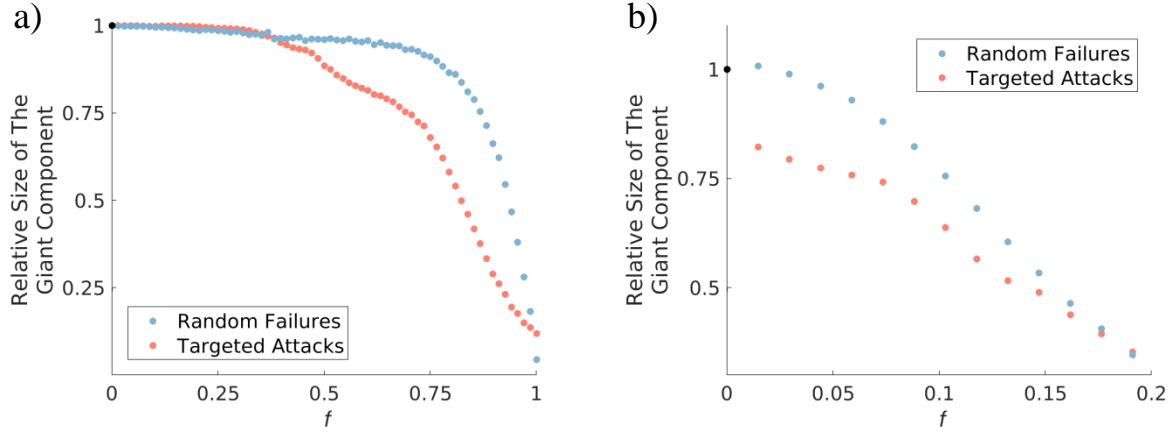


Figure 3. Network breakdown under random failures versus targeted attacks is illustrated for both a liberal (absolute threshold = 0.08) and restrictive (absolute threshold = 0.27) thresholding strategy, respectively in panels (a) and (b). In the case of random failures, the fraction of nodes that belong to the giant component is computed after an f fraction of nodes are randomly selected for perturbation. For a targeted attack, we calculate the fraction of nodes that belong to the giant component after an f fraction of nodes are perturbed in a decreasing order of their hub-score, so that we start with the node with highest hub-score, followed by the next highest etc.

Applying an off-line perturbation protocol to our proposed model enabled us to quantify network vulnerability in the form of hypo-/hyper-connectivity risk rate for either different brain regions/nodes (Figure 4; upper panel) or FCs/links between different functional systems (Figure 4; lower panel). Sub-regions of the cingulate cortex, the temporo-parietal junction (i.e., banks superior temporal sulcus), the parahippocampal cortex (encompassing the parahippocampal gyrus and the fusiform gyrus), the inferior temporal gyrus, the middle frontal gyrus, the inferior parietal cortex (including the inferior parietal gyrus and the angular gyrus) showed a strong risk for hyper-connectivity (Figure 4; uppermost panel, left column). Also, the posterior subdivision of inferior frontal gyrus (pars opercularis) in the right hemisphere, as well as the middle subdivision of inferior frontal gyrus (pars triangularis) in the left hemisphere had strong tendency to increase FC (Figure 4; uppermost panel, left

column). On the other hand, we observed that the regions with the strongest hypo-connectivity risk were located in the posteromedial visual system, frontal pole, medial and lateral orbital frontal cortex, right supramarginal gyrus, right inferior frontal gyrus (pars triangularis and pars orbitalis) and right caudal middle frontal gyrus, and to a lesser extent in the right sensory-motor cortex (post central and precentral gyrus), the right insular cortex and the right superior temporal gyrus as well as left paracentral lobule (Figure 4; upper panel, right column). Furthermore, we observed the highest hyper-connectivity risk for the FC between the VIS system and the SOM and LIM systems, as well as for the CONT/dATT and LIM functional connectivity (Figure 4; lower panel, left column). Additionally, we observed considerable hyper-connectivity risk for the FC between attentional subsystems (SAL/vATT and CONT/dATT), as well as between the SAL/vATT system and the VIS and DM systems, and to a lesser extent between the LIM and SOM systems. The strongest hypo-connectivity risks were found between the DM and VIS, LIM and SAL/vATT, and between the CONT/dATT system with SOM and VIS systems (Figure 4; lower panel, right column).

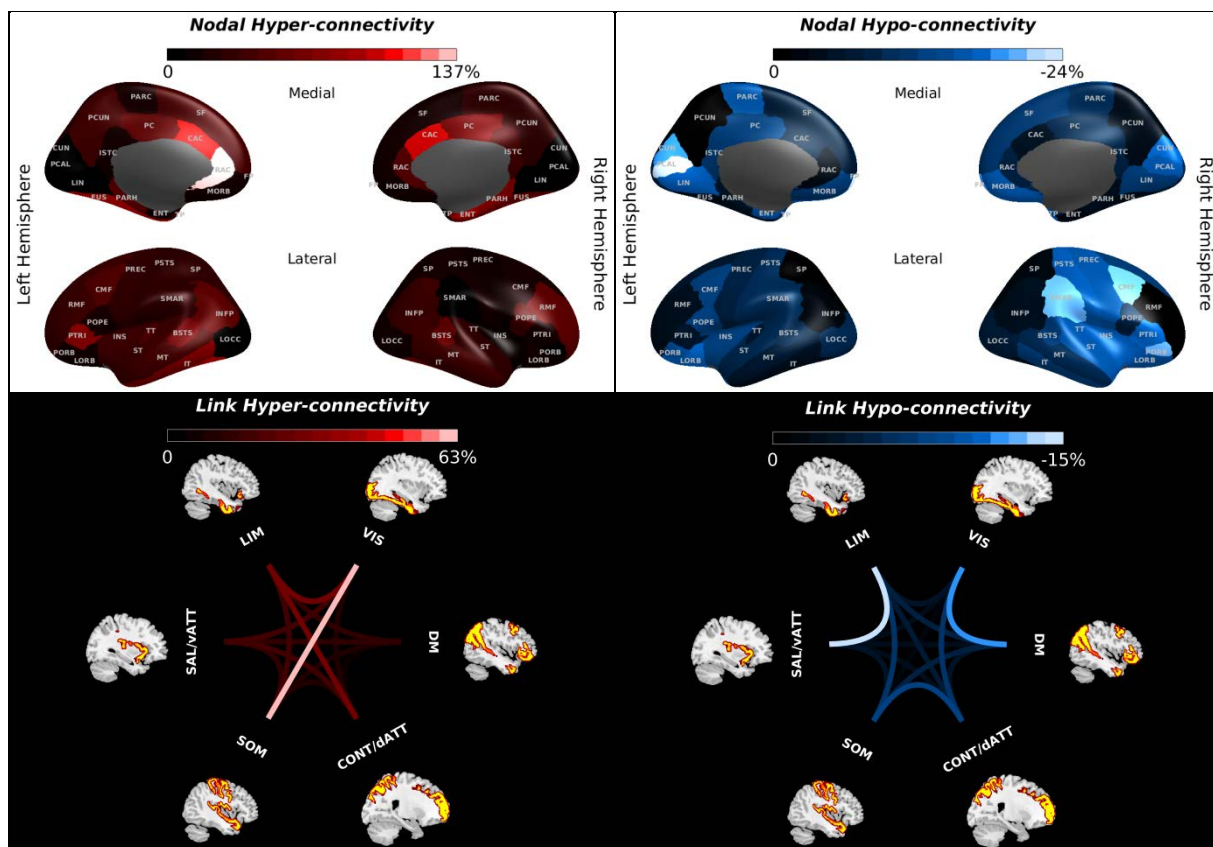


Figure 4. Vulnerability mapping. The upper panel illustrates the vulnerability of different regions. The level of hyper-connectivity risk, which measures the tendency to increase FC in face of distributed failures in the whole brain network, is depicted in the left column, whereas the hypo-connectivity rate as indicative of the tendency to have decreased FC in face of distributed failures in the whole brain network is shown in the right column. The upper panel of this figure shows the nodal risk rate for hyper- and hypo-connectivity in color-format for every node listed in Table 1. The lowermost panel of this figure illustrates the vulnerability of inter-network FCs by color-coded links between different resting-state networks. See Supplementary Table 1 for a list of the abbreviated node names. DM, default mode network (DM); LIM, the limbic system (LIM); dATT/CONT, the dorsal attention or control network; SAL/vATT, the salience or ventral attention network; SOM, the somatomotor network; VIS, the visual network.

Finally, we examined the effects of malfunctions in different brain regions when a combination of local and global measures of brain network as described previously were taken into effect (hazardousness mapping). The results of the hazardousness mapping are shown in Figure 5. In relating the hazardousness measures and the key nodal centrality measures, we found a significant correlation for the clustering coefficient ($r = -0.33$, $p = 0.008$), degree ($r = 0.355$, $p = 0.006$) and strength ($r = 0.39$, $p = 0.004$). Measure of association with hazardousness for the local efficiency was not significant ($r = -0.20$, $p = 0.094$). Reported p values are FDR-corrected across four comparisons.

The analysis of the size of the damage inflicted on the network by applying perturbation to individual nodes showed that the superior parietal cortex (also known as dorsal attention system) and left cuneus cortex, and to a lesser extent the precuneus cortex and the entorhinal cortex were the most critical regions for maintaining adequate network communication. In addition, we observed a high level of hazardousness for some regions in the right hemisphere such as the inferior parietal cortex (including the inferior parietal gyrus and the angular gyrus), the isthmus – cingulate cortex, the middle frontal gyrus, the insular cortex and the caudal anterior-cingulate cortex. Upon closer inspection, the medial orbital frontal cortex and the right posterior-cingulate cortex, as well as the left postcentral gyrus and right parahippocampal gyrus had considerable increased levels of hazardousness (Figure 5). Malfunction in any of the aforementioned areas resulted in a considerable divergence in the brain network characteristics.

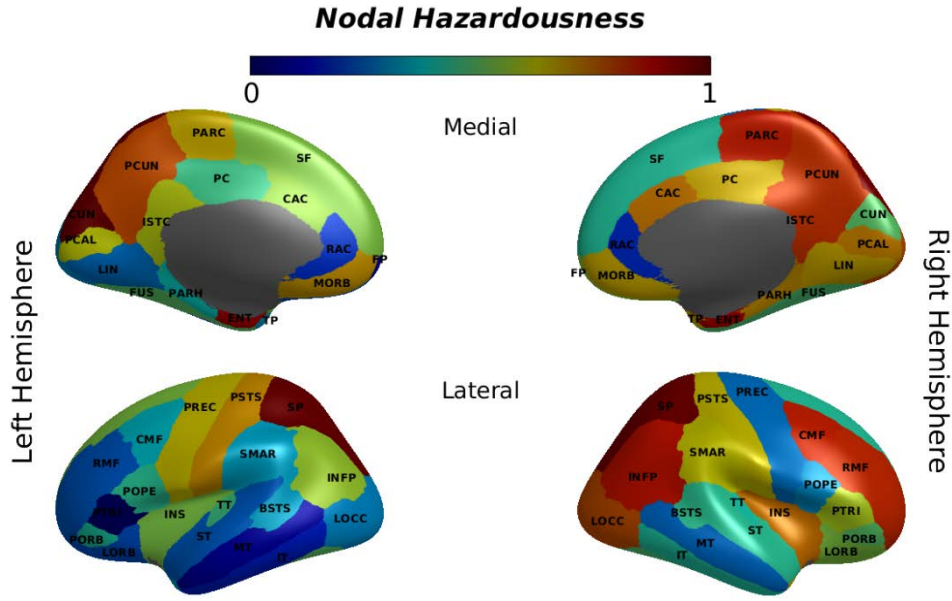


Figure 5. Hazardousness mapping. The degree of hazardousness for a region/node was measured as the degree of feature space divergence from the optimal simulated brain network caused by applying perturbation to that particular node. Normalized measures of distance in feature space are depicted in color-format for every node as listed in Supplementary Table 1. See Supplementary Table 1 for a list of the abbreviated node names.

4. Discussion

4.1. Frequency dynamics

From our results, we conclude that the frequency of region j (i.e., ω_j) undergoes the highest change when the activity in the neighborhood is in the vicinity of zero (Figure 2b). In other words, the slope of frequency change takes its maximum positive value (i.e., speeds up) when the input signals to that region are subsiding, while it experiences a slowdown when the input signals start to grow. Intuitively, this phenomenon may be likened to tuning a radio receiver, to enable it to receive incoming signals from the neighborhood. Thus, the frequency of oscillation of region j (i.e., ω_j), is influenced by the weighted summation of all activities in the neighborhood of region j and it makes ω_j to fluctuate around its intrinsic frequency value, i.e. ω_j^0 . An intuitive interpretation of our suggested dynamic frequency modulation is that

oscillator j intends to stay coupled and keep exchanging information with all of its direct neighbors, as defined by the structural connectome. On the other hand, the state of these oscillators has a time-varying nature, meaning that their position in phase space is changing by time which is captured by their associated angular speed value (as denoted by ω). The acceleration of their displacement (change of phase) is the rate at which ω changes and depends directly upon the “net force”, which is captured by the net phase of ensemble (ψ_j), as an indirect measure of the instantaneous input to oscillator j . Therefore, the global phase of the coupled ensemble to any oscillator modulates the acceleration of its replacement in phase space.

This line of reasoning can be further understood by looking at equation (5) again. The model in equations (5) can be re-written by separating the real and imaginary parts as below ($z_j = x_j + iy_j$):

$$\begin{cases} \dot{x}_j = (a - |x_j|^2 - |y_j|^2)x_j - \omega_j y_j + G \sum C_{ij}(x_i - x_j) + \beta \eta_j \\ \dot{y}_j = (a - |x_j|^2 - |y_j|^2)y_j + \omega_j x_j + G \sum C_{ij}(y_i - y_j) + \beta \eta_j \\ \dot{\omega}_j = \omega_j^0 - \lambda \omega_j + m \psi_j \end{cases} \quad (8)$$

As described in the methods section, we can interpret the real part of variable z (i.e., $x = r \cos \theta$) as the BOLD activity acquired by the MR scanner, whereas the imaginary part (i.e., $y = r \sin \theta$) is interpreted as the hidden state of the system which is undetected by the MR scanner. If the net phase of the neighbor ensemble of region j gets a positive value, which means that the overall neighborhood activity has started to shrink, the steady state of ω_j is greater than $\frac{1}{\lambda} \omega_j^0$. Therefore, receiving a decreasing amount of input from the neighborhood will cause some degree of decline in the weight of the hidden state of z , compared with the intrinsic condition. In the case of a negative net phase for the neighbor ensemble of region j (when the overall neighborhood activity shows a trend of increase), the steady state of ω_j gets

smaller than $\frac{1}{\lambda} \omega^0_j$, leading to an increase in the weight of hidden state compared to the intrinsic condition. This instantaneously splits the oscillators into the sub-groups of oscillators, with either lower or higher weights for their hidden states. We interpret an increase in weight of a hidden state for an oscillator as a higher level of internal processes whereas a lower weight of hidden state may be interpreted as a lower level of internal processes in that particular region.

4.2. Perturbation assessment

4.2.1. Robustness of the whole-brain network model

We observed that the whole-brain network has a lower tolerance when facing selective attacks to central regions. However, in the face of random failures, the fragmentation process was gradual. Indeed, connections in our brain do not arise from a random process. The preferential attachment theory stipulates that there is a higher probability of attachment to nodes that already have high degree values (Barabasi & Albert, 1999). The degree distribution of these networks is better estimated by a power law, rather than a binomial or an exponential distribution. Most of the nodes in a power law distribution have a low degree, whereas some nodes have considerably higher values of degree. Therefore, we cannot select a single brain node to be representative of the others and to give us an estimate of the average degree of the other nodes. Networks following power-law degree distribution are called scale-free networks, since they do not have any characteristic scale (Barabasi & Albert, 1999). In the regular and random networks, the breakdown of the system due to random failure is not a gradual process such that there is an abrupt phase transition from a large connected component to fragmentation, as explained by the inverse percolation theory (Barabási, 2016; Stauffer & Aharony, 1994). Rather, the fragmentation process in the presence of random failures in scale-free networks is gradual. This characteristic makes them

remarkably robust compared to the random and regular networks. However, they are more vulnerable than other types of networks to selective attacks (Barabási, 2016). Although the rich club organization of hubs has been suggested to make them highly robust to failures (van den Heuvel et al., 2012), consecutive attacks to hubs will rather rapidly break the whole-brain network into small disconnected clusters. Therefore, compared with random perturbation, applying selective (ordered by hub score) perturbations to a smaller fraction of regions is sufficient to break down the scale-free network of brain.

4.2.2. Hazardousness mapping

The hazard rates induced by primary failures of individual nodes provide relevant insights not only into the size of the damage inflicted on the network by individual nodes, but also into the potential origin of disease. Our results regarding node hazardousness is interesting in the context of the question why failures in some cases might lead to long-lasting impairment and disease, while other might not. To this end, we observed the highest level of hazardousness for the CONT/dATT system, which mainly covers the superior parietal cortex, right caudal middle frontal gyrus and bilateral rostral middle frontal gyrus, as well as for the posteromedial subsystem of the DM network (particularly the precuneus cortex, the inferior parietal cortex and the isthmus – cingulate cortex). In addition, the LIM system, in particular the entorhinal cortex was found to be a hazardous region. The SAL/vATT system (mostly including the medial subdivisions like posterior cingulate cortex and caudal anterior cingulate, but also the insular cortex) was also found to cause substantial increases in hazardousness levels of damage in case of malfunction (Figure 5). These results substantiate the important role of aforementioned regions for global coordination of information flow across the whole-brain network. It is interesting to note that some of the above mentioned areas with high hazardousness rates overlap with the spatial maps associated with regional controllability of structural brain networks (Gu et al., 2015).

It is also of interest to relate our observation of a high level of hazardousness for the posteromedial subsystem of the DM network, which in the previous literature has been viewed as an important area for integrating the bottom-up attention with behaviorally related information from memory and perception (Andrews-Hanna, Smallwood, & Spreng, 2014). Indeed, previous studies have suggested that the ventral posteromedial cingulate cortex (referred to as the isthmus-cingulate cortex in the Desikan-Killiany atlas) has dense FC that essentially is restricted to the DM network (Kaboodvand et al., 2018; Leech, Kamourieh, Beckmann, & Sharp, 2011; Leech & Sharp, 2014; Spreng, Sepulcre, Turner, Stevens, & Schacter, 2013; Tomasi & Volkow, 2010). Hence, it may be said that it serves as the key provincial hub for the DM network, in that it mediates a large proportion of the traffic that facilitate interactions within this system (Kaboodvand et al., 2018). Moreover, the precuneus/posterior cingulate cortex has been identified as a critical connector hub (Achard et al., 2006; Fransson & Marrelec, 2008; Leech et al., 2011; Spreng et al., 2013; van den Heuvel & Sporns, 2013; Zuo et al., 2012), with dense connections spreading across the whole brain network (Fransson & Marrelec, 2008; Hagmann et al., 2008). FC patterns of the posteromedial subsystem of the DMN have a well-established association with mild cognitive impairment and Alzheimer's disease (Bai et al., 2009; Buckner et al., 2005; Celone et al., 2006; Greicius, Srivastava, Reiss, & Menon, 2004). Positron emission tomography imaging in Alzheimer's disease have shown high amyloid- β deposition in the prominent hubs located in posteromedial cingulate, lateral temporal, lateral parietal, and medial/lateral prefrontal cortices (Buckner et al., 2009; Hedden et al., 2009). There is some evidence suggesting that high level connectedness which is required for large information transfer in the hubs, may cause in augmentation of the underlying pathological cascade in AD (Buckner et al., 2009).

Given that our finding of regions of high hazardousness in the parietal association cortex was predominately right lateralized, it is worthwhile to inquire about the reason for this

asymmetry. Indeed, previous work have reported that lesions of the parietal association cortex in the right hemisphere are more detrimental and that left parietal lesions tend to be compensated by the intact right hemisphere (Purves et al., 2004). Notably, contralateral neglect syndrome is specially associated with damage to the right parietal association cortex. There is evidence suggesting that the right parietal cortex mediates attention to both left and right halves of the body and extra-personal space, whereas the left hemisphere mediates attention primarily to the right side (Purves et al., 2004). There is also strong evidence for the belief that the right middle frontal gyrus is a site of convergence of the dorsal and ventral attention systems, by acting as a circuit-breaker for interrupting ongoing endogenous attentional processes in the dorsal network and reorienting a person's attention to an exogenous task-relevant stimulus (Corbetta, Kincade, & Shulman, 2002; Fox, Corbetta, Snyder, Vincent, & Raichle, 2006; Japee, Holiday, Satyshur, Mukai, & Ungerleider, 2015). Therefore, the right middle frontal gyrus has control over both ventral attention and dorsal attention networks and would be responsible for the flexible modulation of internal and external attention (Corbetta et al., 2002; Fox et al., 2006; Japee et al., 2015).

We found high levels of hazardousness for the entorhinal cortex. This finding resonates well with previous studies that have shown that impairment of the entorhinal cortex is persistently reported in patients with Alzheimer's disease (Van Hoesen, Hyman, & Damasio, 1991), schizophrenia (Arnold, Ruscheinsky, & Han, 1997), as well as in cases of traumatic brain injury and stroke. Moreover, entorhinal damage is believed to cause interference with sensory integration and also cause memory deficits (in particular spatial learning impairment (Van Hoesen et al., 1991)). Moreover, it has been suggested that the age-related entorhinal cortex thinning occurs before hippocampal volume loss and FC decline in the DM system, which impacts communication between medial temporal lobe with the cortical DM system, contributing to age-related memory deficits (Tisserand, Visser, van Boxtel, & Jolles, 2000;

Ward et al., 2015). Of note, it was recently discussed that the entorhinal cortex and retrosplenial cortex (referred as the isthmus – cingulate cortex in the Desikan-Killiany atlas) are sequential interfaces between the medial temporal lobe subsystem of the DM system and cortical regions of the DM system (Kaboodvand et al., 2018). In particular, it was shown that the entorhinal cortex mediates the interaction between medial temporal lobe and the retrosplenial cortex. Therefore, the dynamic coupling/decoupling of the medial temporal lobe from the cortical DM system (Huijbers, Pennartz, Cabeza, & Daselaar, 2011; Vannini et al., 2011; Young & McNaughton, 2009) is mediated by the entorhinal cortex and the retrosplenial cortex together (Kaboodvand et al., 2018). Thus, previous research on the important role for the entorhinal cortex in the brain's network is in well agreement with our findings of an increased level of hazardousness for this region.

Additionally, we found a considerable increased level of hazardousness for right anterior-cingulate cortex. The anterior-cingulate cortex is one of the key integrative brain hubs (Lavin et al., 2013), and it has been suggested to play important role in high-level cognitive processing, outcome monitoring, action planning and emotion processing (Fernández-Matarrubia et al., 2018; Lavin et al., 2013). Furthermore, it acts as a core component in fronto-striatal circuitry. There is evidence that abnormal functioning of right anterior cingulate may have a pathophysiologic role in speech impairment (C.-C. Chang, Lee, Lui, & Lai, 2007) and in the cognitive and emotional impairment related to attention deficit hyperactivity disorder (Tian et al., 2006), schizophrenia (H. Yan et al., 2012) and panic disorder (Shinoura et al., 2011). Notably, there is some evidence in support of FC changes between medial frontal and anterior cingulate in different dementia groups (Fernández-Matarrubia et al., 2018).

4.2.3. Vulnerability mapping

In response to distributed malfunctions (i.e., heterogeneous locations of injury), we observed that functional connections of our brain are obviously more susceptible to risks of hyper-connectivity than hypo-connectivity, particularly in brain regions with high connectedness. Previous studies have repeatedly reported increased functional connectivity after traumatic brain injury as a compensatory brain response to make up for physiological disturbances (Bharath et al., 2015; Hillary et al., 2014; Iraj et al., 2016; Nakamura, Hillary, & Biswal, 2009), particularly so for regions with high connectedness (Hillary et al., 2014). Basically, the observation that “the rich get richer” is in line with the preferential attachment theory underlying scale-free network development, which suggests that new connections mostly occur in the regions with high connectedness (Barabási, 2016). Accumulating evidence have suggested that hyper-connectivity is a common response to neurological disruption in brain insults such as traumatic brain injury, mild cognitive impairment, Alzheimer’s disease, multiple sclerosis and epilepsy (Hillary et al., 2014, 2015). Our nodal vulnerability analysis revealed that the most prominent cases for hyper-connectivity belong to the regions in the default mode, salience, and control systems. More specifically, the anterior-cingulate cortex, the inferior parietal cortex, the left precuneus cortex and also the posterior-cingulate cortex and the middle frontal gyrus, which is consistent with the previous literature on traumatic brain injury (Hillary et al., 2014; Iraj et al., 2016; Mayer, Mannell, Ling, Gasparovic, & Yeo, 2011). For example, increased connections in the acute phase of injury mainly involved the left cingulate gyrus, the left precuneus and the right prefrontal cortices (Bharath et al., 2015; Hillary et al., 2014).

Our results of an increased vulnerability in the fronto-parietal regions is perhaps not overly surprising given that fronto-parietal regions are involved in the top-down attentional control. Interestingly, hyper-connectivity of fronto-parietal regions in the traumatic brain injury

patients is attributed to the increased awareness of the external environment. These observations may explain the reports of cognitive fatigue in these patients (Bharath et al., 2015; Muller & Virji-Babul, 2018; Shumskaya, Andriessen, Norris, & Vos, 2012).

Moreover, previous results suggests that the traumatic brain injury-related hyper-connectivity of the DM system is beneficial for cognitive function (Sharp et al., 2011), in that patients with stronger FC showed the least amount of cognitive impairment. A previous longitudinal study found that during the recovery phase after injury, the weight of network connections (i.e., the strength of hyper-connectivity) diminishes. This finding implies that over the course of recovery, the functional connectome of the injured brain begins to approximate the healthy functional connectome (Nakamura et al., 2009).

Furthermore, there are reports of the decreased FC in the literature which are predominantly right-sided, involving the right frontal and parietal regions (Bharath et al., 2015; Borich, Babul, Yuan, Boyd, & Virji-Babul, 2015; Mayer et al., 2011). For example, the hypo-connectivity for the right supramarginal gyrus and the right middle frontal gyrus, has been reported for the patients with mild brain injury (Borich et al., 2015; Mayer et al., 2011). The lack of dynamic flexibility after traumatic brain injury has been linked to the observed hypo-connectivity of right frontal eye field (Muller & Virji-Babul, 2018).

Our vulnerability mapping suggests that the SAL/vATT system, the CONT/dATT system and the DM system included the regions that had the highest hyper-connectivity risks (e.g., the posterior/anterior- cingulate cortices, the rostral middle frontal and the inferior parietal cortex). On the other hand, we found that the medial visual network, regions of the right parietal lobe (the right supramarginal gyrus and postcentral gyrus), as well as regions of the frontal lobe (caudal middle frontal gyrus, medial and lateral orbital frontal cortex, frontal

pole, pars orbitalis subdivision of the inferior frontal gyrus) had noticeable risks of hypo-connectivity.

Our results regarding the vulnerability of inter-system connections are also in line with the published literature on the effects of injury to brain networks. For example, a previous study of mild traumatic brain injury has reported functional hyper-connectivity for the FC of posterior-cingulate cortex with the frontal eye fields, the dorsolateral prefrontal cortex, the associative visual cortex, the somatosensory association cortex and the premotor cortex, as well as for the FC of occipital lobe with the frontal lobe (Iraji et al., 2016). Our results also indicated considerable level of hyper-connectivity for the SAL/vATT system, encompassing the posterior-cingulate cortex. Of note, there is a body of evidence regarding the hyper-connectivity within the frontal lobe (Bharath et al., 2015; Borich et al., 2015; Hillary et al., 2014; Mayer et al., 2011).

These previous clinical observations give some support to our results of significant hyper-connectivity risks for the FC of SAL/vATT system (which encompasses the posterior-cingulate cortex) with the DM, CONT/dATT, SOM and VIS systems, as well as strong hyper-connectivity between the VIS and LIM systems. Moreover, previous reports of the hyper-connectivity within the frontal lobe (Bharath et al., 2015; Hillary et al., 2014) are of relevance to our observation of strong hyper-connectivity between the CONT system and the limbic or the SAL/vATT systems. Abnormal hyper-connectivity between the top-down attentional systems has been regarded as the underlying cause for some post-traumatic brain injury symptoms, such increased distractibility and cognitive fatigue (Borich et al., 2015; Mayer et al., 2011; Shumskaya et al., 2012).

Taken together, our findings of increased risks of hyper/hypo-connectivity in response to distributed brain failures are largely in agreement with the observations reported in the

aforementioned clinical studies. Thus there are good reasons to believe that the in-silico perturbation assessment of the whole-brain dynamical connectome described here can provide valuable information in predicting re-organization of brain connectivity in response to neurological dysfunctions. In addition, we provided novel evidence for dissimilar susceptibility of FCs when facing heterogeneous failures in the brain network. Moreover, we proposed a method to quantify the regional hazardousness which may serve as a useful index for predicting the impact of specific failures on network characteristics and their damage's contribution in potential long-lasting impairment and disease.(Barabási, 2016)

Acknowledgement

P.F. was supported by the Swedish Research Council (grant No. 2016-03352) and the Swedish e-Science Research Center. Data were provided by the Human Connectome Project, WU-Minn Consortium (Principal Investigators: David Van Essen and Kamil Ugurbil; 1U54MH091657) funded by the 16 NIH Institutes and Centers that support the NIH Blueprint for Neuroscience Research; and by the McDonnell Center for Systems Neuroscience at Washington University. The funders had no role in study design, data collection and analysis, decision to publish, or preparation of the manuscript. The authors thank Behzad Iravani for his valuable methodological advice.

References

- Achard, S., Salvador, R., Whitcher, B., Suckling, J., & Bullmore, E. (2006). A resilient, low-frequency, small-world human brain functional network with highly connected association cortical hubs. *The Journal of Neuroscience*, 26(1), 63–72. doi:10.1523/JNEUROSCI.3874-05.2006
- Andrews-Hanna, J. R., Smallwood, J., & Spreng, R. N. (2014). The default network and self-generated thought: component processes, dynamic control, and clinical relevance. *Annals of the New York Academy of Sciences*, 1316, 29–52. doi:10.1111/nyas.12360
- Arenas, A., Díaz-Guilera, A., Kurths, J., Moreno, Y., & Zhou, C. (2008). Synchronization in complex networks. *Physics Reports*, 469(3), 93–153. doi:10.1016/j.physrep.2008.09.002
- Arnold, S. E., Ruschinsky, D. D., & Han, L. Y. (1997). Further evidence of abnormal cytoarchitecture of the entorhinal cortex in schizophrenia using spatial point pattern analyses. *Biological Psychiatry*, 42(8), 639–647. doi:10.1016/S0006-3223(97)00142-X
- Bai, F., Watson, D. R., Yu, H., Shi, Y., Yuan, Y., & Zhang, Z. (2009). Abnormal resting-state functional connectivity of posterior cingulate cortex in amnesic type mild cognitive impairment. *Brain Research*, 1302, 167–174. doi:10.1016/j.brainres.2009.09.028
- Barabasi, A. L., & Albert, R. (1999). Emergence of scaling in random networks. *Science*, 286(5439), 509–512. doi:10.1126/science.286.5439.509
- Barabási, A.-L. (2016). *Network Science*. Cambridge University Press.
- Betz, R. F., Byrge, L., He, Y., Goñi, J., Zuo, X.-N., & Sporns, O. (2014). Changes in structural and functional connectivity among resting-state networks across the human lifespan. *Neuroimage*, 102 Pt 2, 345–357. doi:10.1016/j.neuroimage.2014.07.067
- Bharath, R. D., Munivenkatappa, A., Gohel, S., Panda, R., Saini, J., Rajeswaran, J., ... Biswal, B. B. (2015). Recovery of resting brain connectivity ensuing mild traumatic brain injury. *Frontiers in Human Neuroscience*, 9, 513. doi:10.3389/fnhum.2015.00513

- Borich, M., Babul, A.-N., Yuan, P. H., Boyd, L., & Virji-Babul, N. (2015). Alterations in resting-state brain networks in concussed adolescent athletes. *Journal of Neurotrauma*, 32(4), 265–271. doi:10.1089/neu.2013.3269
- Breakspear, M. (2017). Dynamic models of large-scale brain activity. *Nature Neuroscience*, 20(3), 340–352. doi:10.1038/nn.4497
- Breakspear, M., Heitmann, S., & Daffertshofer, A. (2010). Generative models of cortical oscillations: neurobiological implications of the kuramoto model. *Frontiers in Human Neuroscience*, 4, 190. doi:10.3389/fnhum.2010.00190
- Buckner, R. L., Sepulcre, J., Talukdar, T., Krienen, F. M., Liu, H., Hedden, T., ... Johnson, K. A. (2009). Cortical hubs revealed by intrinsic functional connectivity: mapping, assessment of stability, and relation to Alzheimer's disease. *The Journal of Neuroscience*, 29(6), 1860–1873. doi:10.1523/JNEUROSCI.5062-08.2009
- Buckner, R. L., Snyder, A. Z., Shannon, B. J., LaRossa, G., Sachs, R., Fotenos, A. F., ... Mintun, M. A. (2005). Molecular, structural, and functional characterization of Alzheimer's disease: evidence for a relationship between default activity, amyloid, and memory. *The Journal of Neuroscience*, 25(34), 7709–7717. doi:10.1523/JNEUROSCI.2177-05.2005
- Cabral, J., Hugues, E., Sporns, O., & Deco, G. (2011). Role of local network oscillations in resting-state functional connectivity. *Neuroimage*, 57(1), 130–139. doi:10.1016/j.neuroimage.2011.04.010
- Cabral, J., Kringelbach, M. L., & Deco, G. (2014). Exploring the network dynamics underlying brain activity during rest. *Progress in Neurobiology*, 114, 102–131. doi:10.1016/j.pneurobio.2013.12.005
- Celone, K. A., Calhoun, V. D., Dickerson, B. C., Atri, A., Chua, E. F., Miller, S. L., ... Sperling, R. A. (2006). Alterations in memory networks in mild cognitive impairment and Alzheimer's disease: an independent component analysis. *The Journal of Neuroscience*, 26(40), 10222–10231. doi:10.1523/JNEUROSCI.2250-06.2006
- Chang, C., & Glover, G. H. (2010). Time-frequency dynamics of resting-state brain connectivity measured with fMRI. *Neuroimage*, 50(1), 81–98. doi:10.1016/j.neuroimage.2009.12.011
- Chang, C.-C., Lee, Y. C., Lui, C.-C., & Lai, S.-L. (2007). Right anterior cingulate cortex infarction and transient speech asponaneity. *Archives of Neurology*, 64(3), 442–446. doi:10.1001/archneur.64.3.442

- Corbetta, M., Kincade, J. M., & Shulman, G. L. (2002). Neural systems for visual orienting and their relationships to spatial working memory. *Journal of Cognitive Neuroscience*, 14(3), 508–523. doi:10.1162/089892902317362029
- Córdova-Palomera, A., Tornador, C., Falcón, C., Bargalló, N., Brambilla, P., Crespo-Facorro, B., ... Fañanás, L. (2016). Environmental factors linked to depression vulnerability are associated with altered cerebellar resting-state synchronization. *Scientific Reports*, 6, 37384. doi:10.1038/srep37384
- De Reus, M. A., & van den Heuvel, M. P. (2013). Estimating false positives and negatives in brain networks. *Neuroimage*, 70, 402–409. doi:10.1016/j.neuroimage.2012.12.066
- Deco, G., & Jirsa, V. K. (2012). Ongoing cortical activity at rest: criticality, multistability, and ghost attractors. *The Journal of Neuroscience*, 32(10), 3366–3375. doi:10.1523/JNEUROSCI.2523-11.2012
- Deco, G., Jirsa, V. K., Robinson, P. A., Breakspear, M., & Friston, K. (2008). The dynamic brain: from spiking neurons to neural masses and cortical fields. *PLoS Computational Biology*, 4(8), e1000092. doi:10.1371/journal.pcbi.1000092
- Deco, G., Jirsa, V., McIntosh, A. R., Sporns, O., & Kötter, R. (2009). Key role of coupling, delay, and noise in resting brain fluctuations. *Proceedings of the National Academy of Sciences of the United States of America*, 106(25), 10302–10307. doi:10.1073/pnas.0901831106
- Deco, G., Kringelbach, M. L., Jirsa, V. K., & Ritter, P. (2017). The dynamics of resting fluctuations in the brain: metastability and its dynamical cortical core. *Scientific Reports*, 7(1), 3095. doi:10.1038/s41598-017-03073-5
- Demirtaş, M., Tornador, C., Falcón, C., López-Solà, M., Hernández-Ribas, R., Pujol, J., ... Deco, G. (2016). Dynamic functional connectivity reveals altered variability in functional connectivity among patients with major depressive disorder. *Human Brain Mapping*, 37(8), 2918–2930. doi:10.1002/hbm.23215
- Desikan, R. S., Ségonne, F., Fischl, B., Quinn, B. T., Dickerson, B. C., Blacker, D., ... Killiany, R. J. (2006). An automated labeling system for subdividing the human cerebral cortex on MRI scans into gyral based regions of interest. *Neuroimage*, 31(3), 968–980. doi:10.1016/j.neuroimage.2006.01.021
- Fernández-Matarrubia, M., Matías-Guiu, J. A., Cabrera-Martín, M. N., Moreno-Ramos, T., Valles-Salgado, M., Carreras, J. L., & Matías-Guiu, J. (2018). Different apathy clinical profile and neural correlates in behavioral variant frontotemporal dementia and Alzheimer's disease. *International Journal of Geriatric Psychiatry*, 33(1), 141–150. doi:10.1002/gps.4695

- Fink, C. G. (2018). Resource Letter PB-1: The Physics of the Brain. *American Journal of Physics*, 86(11), 805–817. doi:10.1119/1.5054288
- Folke, C., Carpenter, S., Walker, B., Scheffer, M., Elmqvist, T., Gunderson, L., & Holling, C. S. (2004). REGIME SHIFTS, RESILIENCE, AND BIODIVERSITY IN ECOSYSTEM MANAGEMENT. *Annual Review of Ecology, Evolution, and Systematics*, 35(1), 557–581. doi:10.1146/annurev.ecolsys.35.021103.105711
- Fornito, A., Zalesky, A., & Bullmore, E. (2016). *Fundamentals of Brain Network Analysis*. Academic Press.
- Fox, M. D., Corbetta, M., Snyder, A. Z., Vincent, J. L., & Raichle, M. E. (2006). Spontaneous neuronal activity distinguishes human dorsal and ventral attention systems. *Proceedings of the National Academy of Sciences of the United States of America*, 103(26), 10046–10051. doi:10.1073/pnas.0604187103
- Fransson, P., & Marrelec, G. (2008). The precuneus/posterior cingulate cortex plays a pivotal role in the default mode network: Evidence from a partial correlation network analysis. *Neuroimage*, 42(3), 1178–1184. doi:10.1016/j.neuroimage.2008.05.059
- Freeman, L. C. (1977). A Set of Measures of Centrality Based on Betweenness. *Sociometry*, 40(1), 35. doi:10.2307/3033543
- Freeman, L. C. (1978). Centrality in social networks conceptual clarification. *Social Networks*, 1(3), 215–239. doi:10.1016/0378-8733(78)90021-7
- Freyer, F., Roberts, J. A., Becker, R., Robinson, P. A., Ritter, P., & Breakspear, M. (2011). Biophysical mechanisms of multistability in resting-state cortical rhythms. *The Journal of Neuroscience*, 31(17), 6353–6361. doi:10.1523/JNEUROSCI.6693-10.2011
- Fukushima, M., Betzel, R. F., He, Y., de Reus, M. A., van den Heuvel, M. P., Zuo, X.-N., & Sporns, O. (2018). Fluctuations between high- and low-modularity topology in time-resolved functional connectivity. *Neuroimage*, 180(Pt B), 406–416. doi:10.1016/j.neuroimage.2017.08.044
- Fukushima, M., Betzel, R. F., He, Y., van den Heuvel, M. P., Zuo, X.-N., & Sporns, O. (2018). Structure-function relationships during segregated and integrated network states of human brain functional connectivity. *Brain Structure & Function*, 223(3), 1091–1106. doi:10.1007/s00429-017-1539-3
- Glasser, M. F., Sotiropoulos, S. N., Wilson, J. A., Coalson, T. S., Fischl, B., Andersson, J. L., ... WU-Minn HCP Consortium. (2013). The minimal preprocessing pipelines for the Human Connectome Project. *Neuroimage*, 80, 105–124. doi:10.1016/j.neuroimage.2013.04.127

- Glerean, E., Salmi, J., Lahnakoski, J. M., Jääskeläinen, I. P., & Sams, M. (2012). Functional magnetic resonance imaging phase synchronization as a measure of dynamic functional connectivity. *Brain Connectivity*, 2(2), 91–101. doi:10.1089/brain.2011.0068
- Gollo, L. L., Roberts, J. A., Copley, V. L., Di Biase, M. A., Pantelis, C., Zalesky, A., & Breakspear, M. (2018). Fragility and volatility of structural hubs in the human connectome. *Nature Neuroscience*, 21(8), 1107–1116. doi:10.1038/s41593-018-0188-z
- Gollo, L. L., Zalesky, A., Hutchison, R. M., van den Heuvel, M., & Breakspear, M. (2015). Dwelling quietly in the rich club: brain network determinants of slow cortical fluctuations. *Philosophical Transactions of the Royal Society of London. Series B, Biological Sciences*, 370(1668). doi:10.1098/rstb.2014.0165
- Greicius, M. D., Srivastava, G., Reiss, A. L., & Menon, V. (2004). Default-mode network activity distinguishes Alzheimer's disease from healthy aging: evidence from functional MRI. *Proceedings of the National Academy of Sciences of the United States of America*, 101(13), 4637–4642. doi:10.1073/pnas.0308627101
- Griffa, A., Baumann, P. S., Thiran, J.-P., & Hagmann, P. (2013). Structural connectomics in brain diseases. *Neuroimage*, 80, 515–526. doi:10.1016/j.neuroimage.2013.04.056
- Griffanti, L., Salimi-Khorshidi, G., Beckmann, C. F., Auerbach, E. J., Douaud, G., Sexton, C. E., ... Smith, S. M. (2014). ICA-based artefact removal and accelerated fMRI acquisition for improved resting state network imaging. *Neuroimage*, 95, 232–247. doi:10.1016/j.neuroimage.2014.03.034
- Gu, S., Pasqualetti, F., Cieslak, M., Telesford, Q. K., Yu, A. B., Kahn, A. E., ... Bassett, D. S. (2015). Controllability of structural brain networks. *Nature Communications*, 6, 8414. doi:10.1038/ncomms9414
- Hagmann, P., Cammoun, L., Gigandet, X., Meuli, R., Honey, C. J., Wedeen, V. J., & Sporns, O. (2008). Mapping the structural core of human cerebral cortex. *PLoS Biology*, 6(7), e159. doi:10.1371/journal.pbio.0060159
- Harary, F. (1969). *Graph theory*. (F. Harary, Ed.) (illustrated, reprint.). Addison-Wesley Pub. Co.
- Hedden, T., Van Dijk, K. R. A., Becker, J. A., Mehta, A., Sperling, R. A., Johnson, K. A., & Buckner, R. L. (2009). Disruption of functional connectivity in clinically normal older adults harboring amyloid burden. *The Journal of Neuroscience*, 29(40), 12686–12694. doi:10.1523/JNEUROSCI.3189-09.2009
- Hilborn, R. C. (2000). *Chaos and nonlinear dynamics*. Oxford University Press. doi:10.1093/acprof:oso/9780198507239.001.0001

- Hillary, F. G., Rajtmajer, S. M., Roman, C. A., Medaglia, J. D., Slocomb-Dluzen, J. E., Calhoun, V. D., ... Wylie, G. R. (2014). The rich get richer: brain injury elicits hyperconnectivity in core subnetworks. *Plos One*, 9(8), e104021. doi:10.1371/journal.pone.0104021
- Hillary, F. G., Roman, C. A., Venkatesan, U., Rajtmajer, S. M., Bajo, R., & Castellanos, N. D. (2015). Hyperconnectivity is a fundamental response to neurological disruption. *Neuropsychology*, 29(1), 59–75. doi:10.1037/neu0000110
- Holling, C. S. (1973). Resilience and Stability of Ecological Systems. *Annual Review of Ecology and Systematics*, 4(1), 1–23. doi:10.1146/annurev.es.04.110173.000245
- Honey, C J, Sporns, O., Cammoun, L., Gigandet, X., Thiran, J. P., Meuli, R., & Hagmann, P. (2009). Predicting human resting-state functional connectivity from structural connectivity. *Proceedings of the National Academy of Sciences of the United States of America*, 106(6), 2035–2040. doi:10.1073/pnas.0811168106
- Honey, Christopher J, Kötter, R., Breakspear, M., & Sporns, O. (2007). Network structure of cerebral cortex shapes functional connectivity on multiple time scales. *Proceedings of the National Academy of Sciences of the United States of America*, 104(24), 10240–10245. doi:10.1073/pnas.0701519104
- Huijbers, W., Pennartz, C. M. A., Cabeza, R., & Daselaar, S. M. (2011). The hippocampus is coupled with the default network during memory retrieval but not during memory encoding. *Plos One*, 6(4), e17463. doi:10.1371/journal.pone.0017463
- Hutchison, R. M., Womelsdorf, T., Allen, E. A., Bandettini, P. A., Calhoun, V. D., Corbetta, M., ... Chang, C. (2013). Dynamic functional connectivity: promise, issues, and interpretations. *Neuroimage*, 80, 360–378. doi:10.1016/j.neuroimage.2013.05.079
- Iraji, A., Chen, H., Wiseman, N., Welch, R. D., O’Neil, B. J., Haacke, E. M., ... Kou, Z. (2016). Compensation through Functional Hyperconnectivity: A Longitudinal Connectome Assessment of Mild Traumatic Brain Injury. *Neural Plasticity*, 2016, 4072402. doi:10.1155/2016/4072402
- Japee, S., Holiday, K., Satyshur, M. D., Mukai, I., & Ungerleider, L. G. (2015). A role of right middle frontal gyrus in reorienting of attention: a case study. *Frontiers in Systems Neuroscience*, 9, 23. doi:10.3389/fnsys.2015.00023
- Kaboodvand, N., Bäckman, L., Nyberg, L., & Salami, A. (2018). The retrosplenial cortex: A memory gateway between the cortical default mode network and the medial temporal lobe. *Human Brain Mapping*, 39(5), 2020–2034. doi:10.1002/hbm.23983

- Kelso, J. A. S. (2008). An essay on understanding the mind. *Ecological Psychology : a Publication of the International Society for Ecological Psychology*, 20(2), 180–208. doi:10.1080/10407410801949297
- Kuramoto, Y. (1984). *Chemical oscillations, waves, and turbulence* (Vol. 19). Berlin, Heidelberg: Springer Berlin Heidelberg. doi:10.1007/978-3-642-69689-3
- Lavin, C., Melis, C., Mikulan, E., Gelormini, C., Huepe, D., & Ibañez, A. (2013). The anterior cingulate cortex: an integrative hub for human socially-driven interactions. *Frontiers in Neuroscience*, 7, 64. doi:10.3389/fnins.2013.00064
- Leech, R., Kamourieh, S., Beckmann, C. F., & Sharp, D. J. (2011). Fractionating the default mode network: distinct contributions of the ventral and dorsal posterior cingulate cortex to cognitive control. *The Journal of Neuroscience*, 31(9), 3217–3224. doi:10.1523/JNEUROSCI.5626-10.2011
- Leech, R., & Sharp, D. J. (2014). The role of the posterior cingulate cortex in cognition and disease. *Brain: A Journal of Neurology*, 137(Pt 1), 12–32. doi:10.1093/brain/awt162
- Mayer, A. R., Mannell, M. V., Ling, J., Gasparovic, C., & Yeo, R. A. (2011). Functional connectivity in mild traumatic brain injury. *Human Brain Mapping*, 32(11), 1825–1835. doi:10.1002/hbm.21151
- Meunier, D., Lambiotte, R., Fornito, A., Ersche, K. D., & Bullmore, E. T. (2009). Hierarchical modularity in human brain functional networks. *Frontiers in Neuroinformatics*, 3, 37. doi:10.3389/neuro.11.037.2009
- Muller, A. M., & Virji-Babul, N. (2018). Stuck in a state of inattention? functional hyperconnectivity as an indicator of disturbed intrinsic brain dynamics in adolescents with concussion: A pilot study. *ASN Neuro*, 10, 1759091417753802. doi:10.1177/1759091417753802
- Nakamura, T., Hillary, F. G., & Biswal, B. B. (2009). Resting network plasticity following brain injury. *Plos One*, 4(12), e8220. doi:10.1371/journal.pone.0008220
- Newman, M., Barabási, A.-L., & Watts, D. J. (2011). *The Structure and Dynamics of Networks* (illustrated.). Princeton University Press.
- Newman, M. E. J. (2003). The Structure and Function of Complex Networks. *SIAM Review*, 45, 167–256. doi:10.1137/S003614450342480
- Omidvarnia, A., Pedersen, M., Walz, J. M., Vaughan, D. N., Abbott, D. F., & Jackson, G. D. (2016). Dynamic regional phase synchrony (DRePS): An Instantaneous Measure of Local fMRI Connectivity Within Spatially Clustered Brain Areas. *Human Brain Mapping*, 37(5), 1970–1985. doi:10.1002/hbm.23151

- Pedersen, M., Omidvarnia, A., Walz, J. M., Zalesky, A., & Jackson, G. D. (2017). Spontaneous brain network activity: Analysis of its temporal complexity. *Network Neuroscience (Cambridge, Mass.)*, 1(2), 100–115. doi:10.1162/NETN_a_00006
- Pedersen, M., Omidvarnia, A., Zalesky, A., & Jackson, G. D. (2017). On the relationship between instantaneous phase synchrony and correlation-based sliding windows for time-resolved fMRI connectivity analysis. *BioRxiv*. doi:10.1101/179820
- Ponce-Alvarez, A., Deco, G., Hagmann, P., Romani, G. L., Mantini, D., & Corbetta, M. (2015). Resting-state temporal synchronization networks emerge from connectivity topology and heterogeneity. *PLoS Computational Biology*, 11(2), e1004100. doi:10.1371/journal.pcbi.1004100
- Power, J. D., Cohen, A. L., Nelson, S. M., Wig, G. S., Barnes, K. A., Church, J. A., ... Petersen, S. E. (2011). Functional network organization of the human brain. *Neuron*, 72(4), 665–678. doi:10.1016/j.neuron.2011.09.006
- Purves, D., Augustine, G., Fitzpatrick, D., Hall, W., LaMantia, A., White, L., ... Platt, M. (2004). *Neuroscience*. (D. Purves, G. Augustine, D. Fitzpatrick, W. Hall, A. LaMantia, L. White, ... M. Platt, Eds.) (3rd ed.). Sunderland, MA 01375 U.S.A.: Oxford University Press.
- Ries, A., Chang, C., Glim, S., Meng, C., Sorg, C., & Wohlschläger, A. (2018). Grading of Frequency Spectral Centroid Across Resting-State Networks. *Frontiers in Human Neuroscience*, 12, 436. doi:10.3389/fnhum.2018.00436
- Ritter, P., Schirner, M., McIntosh, A. R., & Jirsa, V. K. (2013). The virtual brain integrates computational modeling and multimodal neuroimaging. *Brain Connectivity*, 3(2), 121–145. doi:10.1089/brain.2012.0120
- Roberts, J. A., Friston, K. J., & Breakspear, M. (2017). Clinical applications of stochastic dynamic models of the brain, part I: A primer. *Biological Psychiatry: Cognitive Neuroscience and Neuroimaging*, 2(3), 216–224. doi:10.1016/j.bpsc.2017.01.010
- Roberts, J. A., Gollo, L. L., Abeysuriya, R., Roberts, G., Mitchell, P. B., Woolrich, M. W., & Breakspear, M. (2018). Metastable brain waves. *BioRxiv*. doi:10.1101/347054
- Rodrigues, F. A., Peron, T. K. D., Ji, P., & Kurths, J. (2016). The Kuramoto model in complex networks. *Physics Reports*, 610, 1–98. doi:10.1016/j.physrep.2015.10.008
- Rubinov, M., & Sporns, O. (2010). Complex network measures of brain connectivity: uses and interpretations. *Neuroimage*, 52(3), 1059–1069. doi:10.1016/j.neuroimage.2009.10.003

- Rubinov, M., & Sporns, O. (2011). Weight-conserving characterization of complex functional brain networks. *Neuroimage*, 56(4), 2068–2079. doi:10.1016/j.neuroimage.2011.03.069
- Röhm, A., Lüdge, K., & Schneider, I. (2018). Bistability in two simple symmetrically coupled oscillators with symmetry-broken amplitude- and phase-locking. *Chaos*, 28(6), 063114. doi:10.1063/1.5018262
- Salimi-Khorshidi, G., Douaud, G., Beckmann, C. F., Glasser, M. F., Griffanti, L., & Smith, S. M. (2014). Automatic denoising of functional MRI data: combining independent component analysis and hierarchical fusion of classifiers. *Neuroimage*, 90, 449–468. doi:10.1016/j.neuroimage.2013.11.046
- Scheffer, M., Carpenter, S., Foley, J. A., Folke, C., & Walker, B. (2001). Catastrophic shifts in ecosystems. *Nature*, 413(6856), 591–596. doi:10.1038/35098000
- Senden, M., Reuter, N., van den Heuvel, M. P., Goebel, R., & Deco, G. (2017). Cortical rich club regions can organize state-dependent functional network formation by engaging in oscillatory behavior. *Neuroimage*, 146, 561–574. doi:10.1016/j.neuroimage.2016.10.044
- Sharp, D. J., Beckmann, C. F., Greenwood, R., Kinnunen, K. M., Bonnelle, V., De Boissezon, X., ... Leech, R. (2011). Default mode network functional and structural connectivity after traumatic brain injury. *Brain: A Journal of Neurology*, 134(Pt 8), 2233–2247. doi:10.1093/brain/awr175
- Shinoura, N., Yamada, R., Tabei, Y., Otani, R., Itoi, C., Saito, S., & Midorikawa, A. (2011). Damage to the right dorsal anterior cingulate cortex induces panic disorder. *Journal of Affective Disorders*, 133(3), 569–572. doi:10.1016/j.jad.2011.04.029
- Shumskaya, E., Andriessen, T. M. J. C., Norris, D. G., & Vos, P. E. (2012). Abnormal whole-brain functional networks in homogeneous acute mild traumatic brain injury. *Neurology*, 79(2), 175–182. doi:10.1212/WNL.0b013e31825f04fb
- Skardal, P. S., Ott, E., & Restrepo, J. G. (2011). Cluster synchrony in systems of coupled phase oscillators with higher-order coupling. *Physical Review. E, Statistical, Nonlinear, and Soft Matter Physics*, 84(3 Pt 2), 036208. doi:10.1103/PhysRevE.84.036208
- Smith, S. M., Beckmann, C. F., Andersson, J., Auerbach, E. J., Bijsterbosch, J., Douaud, G., ... WU-Minn HCP Consortium. (2013). Resting-state fMRI in the Human Connectome Project. *Neuroimage*, 80, 144–168. doi:10.1016/j.neuroimage.2013.05.039
- Smith, S. M., Fox, P. T., Miller, K. L., Glahn, D. C., Fox, P. M., Mackay, C. E., ... Beckmann, C. F. (2009). Correspondence of the brain's functional architecture during activation and rest. *Proceedings of the National Academy of Sciences of*

the United States of America, 106(31), 13040–13045.
doi:10.1073/pnas.0905267106

- Sporns, O., Honey, C. J., & Kötter, R. (2007). Identification and classification of hubs in brain networks. *Plos One*, 2(10), e1049. doi:10.1371/journal.pone.0001049
- Spreng, R. N., Sepulcre, J., Turner, G. R., Stevens, W. D., & Schacter, D. L. (2013). Intrinsic architecture underlying the relations among the default, dorsal attention, and frontoparietal control networks of the human brain. *Journal of Cognitive Neuroscience*, 25(1), 74–86. doi:10.1162/jocn_a_00281
- Stauffer, D., & Aharony, A. (1994). *Introduction To Percolation Theory*. CRC Press.
- Strogatz, S. H. (2001). Exploring complex networks. *Nature*, 410, 268–276.
doi:10.1038/35065725
- Strogatz, Steven H. (2018). *Nonlinear dynamics and chaos: with applications to physics, biology, chemistry, and engineering*. CRC Press. doi:10.1201/9780429492563
- Thompson, W. H., Brantefors, P., & Fransson, P. (2017). From static to temporal network theory: Applications to functional brain connectivity. *Network Neuroscience (Cambridge, Mass.)*, 1(2), 69–99. doi:10.1162/NETN_a_00011
- Thompson, W. H., & Fransson, P. (2015). The frequency dimension of fMRI dynamic connectivity: Network connectivity, functional hubs and integration in the resting brain. *Neuroimage*, 121, 227–242.
doi:10.1016/j.neuroimage.2015.07.022
- Tian, L., Jiang, T., Wang, Y., Zang, Y., He, Y., Liang, M., ... Zhuo, Y. (2006). Altered resting-state functional connectivity patterns of anterior cingulate cortex in adolescents with attention deficit hyperactivity disorder. *Neuroscience Letters*, 400(1-2), 39–43. doi:10.1016/j.neulet.2006.02.022
- Tisserand, D. J., Visser, P. J., van Boxtel, M. P., & Jolles, J. (2000). The relation between global and limbic brain volumes on MRI and cognitive performance in healthy individuals across the age range. *Neurobiology of Aging*, 21(4), 569–576.
- Tognoli, E., & Kelso, J. A. S. (2014). The metastable brain. *Neuron*, 81(1), 35–48.
doi:10.1016/j.neuron.2013.12.022
- Tomasi, D., & Volkow, N. D. (2010). Functional connectivity density mapping. *Proceedings of the National Academy of Sciences of the United States of America*, 107(21), 9885–9890. doi:10.1073/pnas.1001414107
- Van den Heuvel, M. P., de Reus, M. A., Feldman Barrett, L., Scholtens, L. H., Coopmans, F. M. T., Schmidt, R., ... Li, L. (2015). Comparison of diffusion tractography and tract-tracing measures of connectivity strength in rhesus macaque connectome. *Human Brain Mapping*, 36(8), 3064–3075. doi:10.1002/hbm.22828

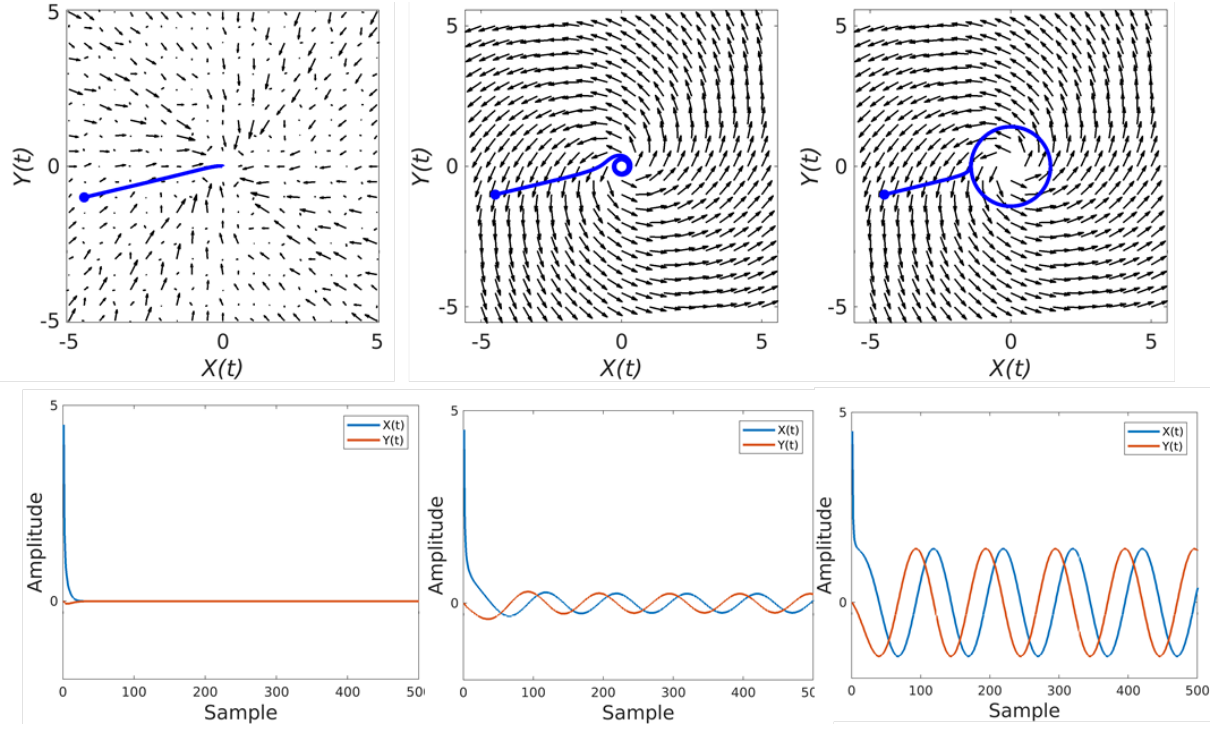
- Van den Heuvel, M. P., Kahn, R. S., Goñi, J., & Sporns, O. (2012). High-cost, high-capacity backbone for global brain communication. *Proceedings of the National Academy of Sciences of the United States of America*, 109(28), 11372–11377. doi:10.1073/pnas.1203593109
- Van den Heuvel, M. P., & Sporns, O. (2011). Rich-club organization of the human connectome. *The Journal of Neuroscience*, 31(44), 15775–15786. doi:10.1523/JNEUROSCI.3539-11.2011
- Van den Heuvel, M. P., & Sporns, O. (2013). Network hubs in the human brain. *Trends in Cognitive Sciences*, 17(12), 683–696. doi:10.1016/j.tics.2013.09.012
- Van Essen, D. C., Ugurbil, K., Auerbach, E., Barch, D., Behrens, T. E. J., Bucholz, R., ... WU-Minn HCP Consortium. (2012). The Human Connectome Project: a data acquisition perspective. *Neuroimage*, 62(4), 2222–2231. doi:10.1016/j.neuroimage.2012.02.018
- Van Hoesen, G. W., Hyman, B. T., & Damasio, A. R. (1991). Entorhinal cortex pathology in Alzheimer's disease. *Hippocampus*, 1(1), 1–8. doi:10.1002/hipo.450010102
- Vannini, P., O'Brien, J., O'Keefe, K., Pihlajamäki, M., Laviolette, P., & Sperling, R. A. (2011). What goes down must come up: role of the posteromedial cortices in encoding and retrieval. *Cerebral Cortex*, 21(1), 22–34. doi:10.1093/cercor/bhq051
- Ward, A. M., Mormino, E. C., Huijbers, W., Schultz, A. P., Hedden, T., & Sperling, R. A. (2015). Relationships between default-mode network connectivity, medial temporal lobe structure, and age-related memory deficits. *Neurobiology of Aging*, 36(1), 265–272. doi:10.1016/j.neurobiolaging.2014.06.028
- Váša, F., Shanahan, M., Hellyer, P. J., Scott, G., Cabral, J., & Leech, R. (2015). Effects of lesions on synchrony and metastability in cortical networks. *Neuroimage*, 118, 456–467. doi:10.1016/j.neuroimage.2015.05.042
- Weerasinghe, G., Duchet, B., Cagnan, H., Brown, P., Bick, C., & Bogacz, R. (2018). Predicting the effects of deep brain stimulation using a reduced coupled oscillator model. *BioRxiv*. doi:10.1101/448290
- Yaesoubi, M., Allen, E. A., Miller, R. L., & Calhoun, V. D. (2015). Dynamic coherence analysis of resting fMRI data to jointly capture state-based phase, frequency, and time-domain information. *Neuroimage*, 120, 133–142. doi:10.1016/j.neuroimage.2015.07.002
- Yan, C.-G., Craddock, R. C., Zuo, X.-N., Zang, Y.-F., & Milham, M. P. (2013). Standardizing the intrinsic brain: towards robust measurement of inter-individual variation in 1000 functional connectomes. *Neuroimage*, 80, 246–262. doi:10.1016/j.neuroimage.2013.04.081

- Yan, H., Tian, L., Yan, J., Sun, W., Liu, Q., Zhang, Y.-B., ... Zhang, D. (2012). Functional and anatomical connectivity abnormalities in cognitive division of anterior cingulate cortex in schizophrenia. *Plos One*, 7(9), e45659. doi:10.1371/journal.pone.0045659
- Yeh, F.-C., Wedeen, V. J., & Tseng, W.-Y. I. (2010). Generalized q-sampling imaging. *IEEE Transactions on Medical Imaging*, 29(9), 1626–1635. doi:10.1109/TMI.2010.2045126
- Yeo, B. T. T., Krienen, F. M., Sepulcre, J., Sabuncu, M. R., Lashkari, D., Hollinshead, M., ... Buckner, R. L. (2011). The organization of the human cerebral cortex estimated by intrinsic functional connectivity. *Journal of Neurophysiology*, 106(3), 1125–1165. doi:10.1152/jn.00338.2011
- Young, C. K., & McNaughton, N. (2009). Coupling of theta oscillations between anterior and posterior midline cortex and with the hippocampus in freely behaving rats. *Cerebral Cortex*, 19(1), 24–40. doi:10.1093/cercor/bhn055
- Zalesky, A., Fornito, A., Cocchi, L., Gollo, L. L., & Breakspear, M. (2014). Time-resolved resting-state brain networks. *Proceedings of the National Academy of Sciences of the United States of America*, 111(28), 10341–10346. doi:10.1073/pnas.1400181111
- Zuo, X.-N., Ehmke, R., Mennes, M., Imperati, D., Castellanos, F. X., Sporns, O., & Milham, M. P. (2012). Network centrality in the human functional connectome. *Cerebral Cortex*, 22(8), 1862–1875. doi:10.1093/cercor/bhr269

Supplementary Material

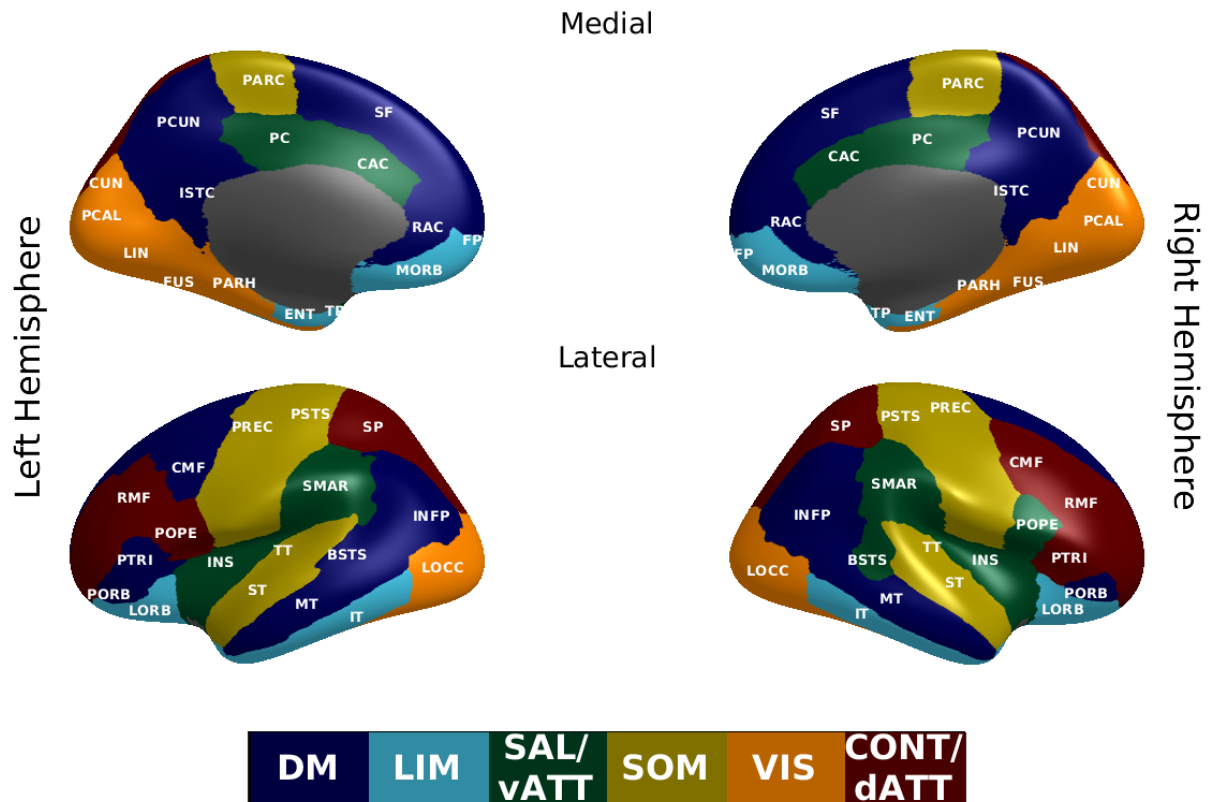
Supplementary Table 1. The list of abbreviations and complete names for all 68 regions-of-interest as included in the 'Desikan-Killiany' cortical atlas are shown in the table.

Abbreviation	Complete Name
BSTS	Banks superior temporal sulcus
CAC	Caudal anterior-cingulate cortex
CMF	Caudal middle frontal gyrus
CUN	Cuneus cortex
ENT	Entorhinal cortex
FUS	Fusiform gyrus
INFP	Inferior parietal cortex
IT	Inferior temporal gyrus
ISTC	Isthmus – cingulate cortex
LOCC	Lateral occipital cortex
LORB	Lateral orbital frontal cortex
LIN	Lingual gyrus
MORB	Medial orbital frontal cortex
MT	Middle temporal gyrus
PARH	Parahippocampal gyrus
PARC	Paracentral lobule
POPE	Pars opercularis
PORB	Pars orbitalis
PTRI	Pars triangularis
PCAL	Pericalcarine cortex
PSTS	Postcentral gyrus
PC	Posterior-cingulate cortex
PREC	Precentral gyrus
PCUN	Precuneus cortex
RAC	Rostral anterior cingulate cortex
RMF	Rostral middle frontal gyrus
SF	Superior frontal gyrus
SP	Superior parietal cortex
ST	Superior temporal gyrus
SMAR	Supramarginal gyrus
FP	Frontal pole
TP	Temporal pole
TT	Transverse temporal cortex
INS	Insular cortex

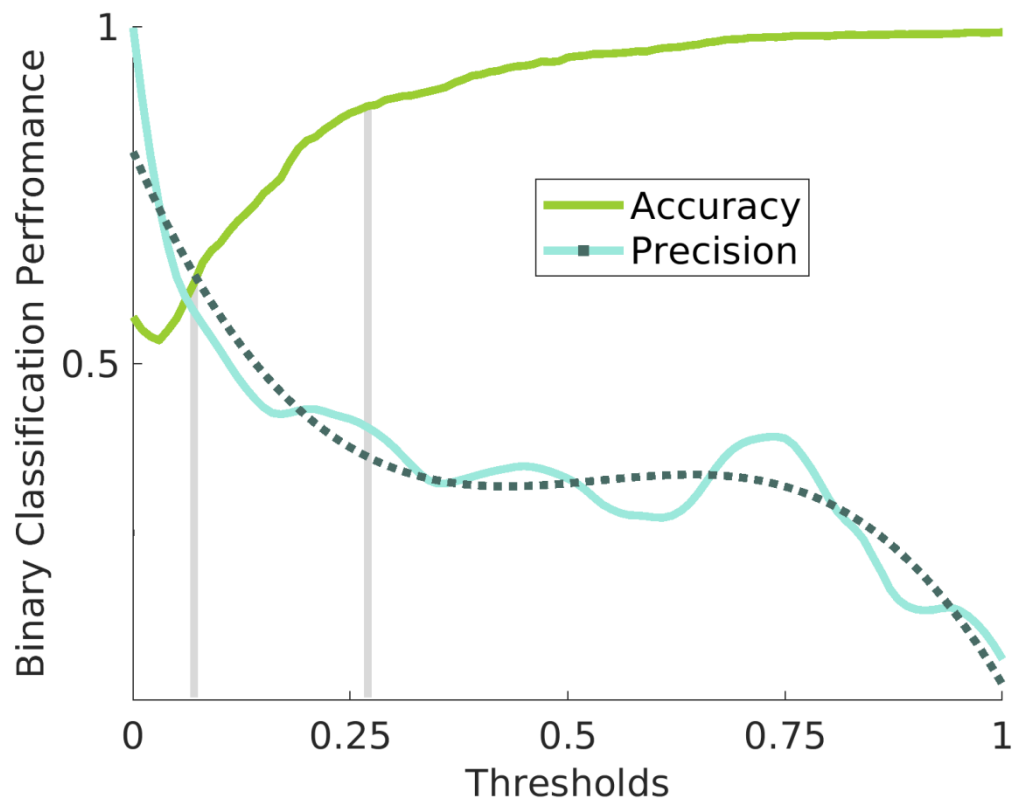


Supplementary Figure 1. An illustrative example of phase space vector fields as well as temporal evolution of the Stuart-Landau oscillator. where $\mathbf{z} = \mathbf{r} e^{i\theta} = \mathbf{x} + i\mathbf{y}$ is a complex number describing the state of the oscillator, $\omega \in \mathbb{R}$ is the frequency of each oscillator and the bifurcation parameter $\mathbf{a} \in \mathbb{R}$ determines whether the oscillator is characterized by noisy fluctuations or exhibits oscillatory behavior. The origin (i.e., $\mathbf{z} = \mathbf{0}$) is the fixed point of this system. The eigenvalues of this system all have complex conjugate values ($\sigma = \mathbf{a} \pm i\omega$), indicating a spiral trajectory behavior in the neighborhood of the fixed point in phase space. If $\mathbf{a} < \mathbf{0}$, then the origin is a stable equilibrium solution with solutions spiraling into the origin (as illustrated in the first column of the figure). However, if $\mathbf{a} > \mathbf{0}$, then the origin is an unstable equilibrium with solutions spiraling out from the origin (as illustrated in the third column of the figure). The illustrated closed orbit in the phase space represents the periodic behavior of the system. Solutions that reside inside of the closed orbit will spiral out towards the orbit, while solutions outside of the orbit will spiral inward. The middle column includes an example phase space and the associated signals at the bifurcation point ($\mathbf{a} = \mathbf{0}$).

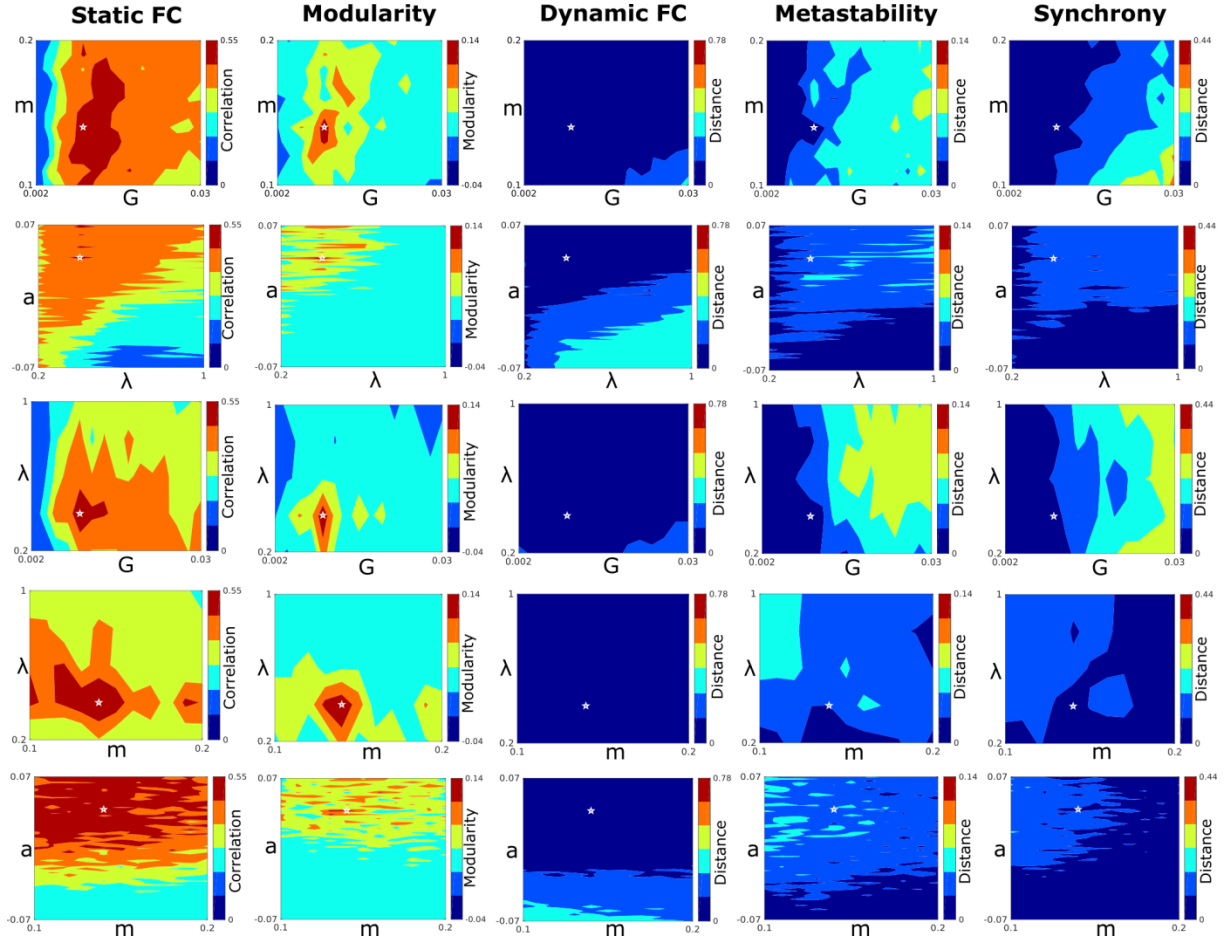
Resting State Networks



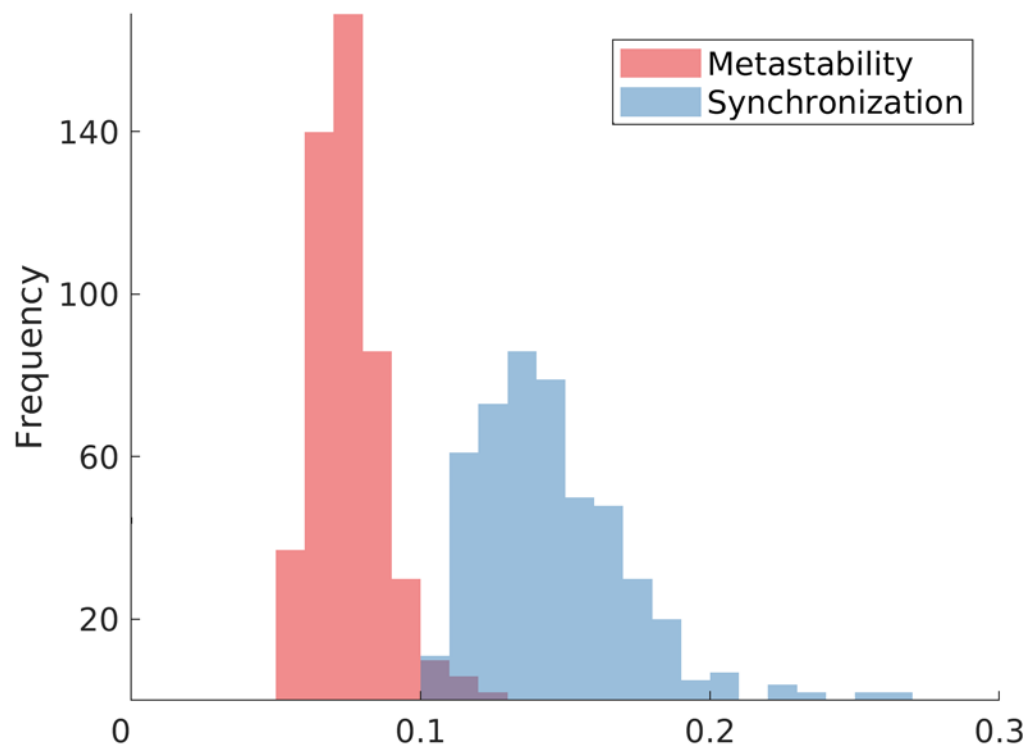
Supplementary Figure 2. The layout of the functional networks. The used abbreviations for brain regions are shown in Supplementary Table 1. DM, default mode network (DM); LIM, the limbic system (LIM); dATT/CONT, the dorsal attention or control network; SAL/vATT, the salience or ventral attention network; SOM, the somatomotor network; VIS, the visual network.



Supplementary Figure 3. The accuracy and precision of the binary classification of edges at different thresholds ranging from 0 to 1 are illustrated. Cubic polynomial curve fitted to the precision is depicted as the dotted green curve. The locations of the intersection of two performance measures, as well as the knee point for both curves refer to the thresholds of 0.08 and 0.27, respectively.



Supplementary Figure 4. Parameter space search. This figure shows the exploration of the parameter space defined by the bifurcation parameter a , global coupling G , frequency lethargy λ and frequency modulation m . First column depicts the Pearson correlation between empirical and simulated static FC patterns for different pairings of parameters. Second column shows the whole brain modularity computed for the simulated static FC matrix. The Kolmogorov-Smirnoff distance between cumulative distributions of the pairwise similarity among instantaneous FC values, obtained from the empirical and simulated BOLD signals, as well as the difference of metastability and synchrony of simulated signals from the average metastability and synchrony measures of empirical BOLD signals are respectively illustrated in columns 3-5. Measures associated with the optimal choice of global coupling (G), bifurcation parameter (a), frequency lethargy λ and frequency modulation m are shown as a white asterisk ($G=0.01$, $a=0.038$, $\lambda=0.4$ and $m=0.14$).



Supplementary Figure 5. The distribution of global synchrony and global metastability as indicative of macroscopic coherence of the whole-brain network are illustrated for the empirical BOLD signals.